

Mixed-precision finite element kernels and assembly: Rounding error analysis and hardware acceleration

Matteo Croci*

Garth N. Wells†

Abstract

In this paper we develop the first fine-grained rounding error analysis of finite element (FE) cell kernels and assembly. The theory includes mixed-precision implementations and accounts for hardware-acceleration via matrix multiplication units, thus providing theoretical guidance for designing reduced- and mixed-precision FE algorithms on CPUs and GPUs. Guided by this analysis, we introduce hardware-accelerated mixed-precision implementation strategies which are provably robust to low-precision computations. Indeed, these algorithms are accurate to the lower-precision unit roundoff with an error constant that is independent from: the conditioning of FE basis function evaluations, the ill-posedness of the cell, the polynomial degree, and the number of quadrature nodes. Consequently, we present the first AMX-accelerated FE kernel implementations on Intel Sapphire Rapids CPUs. Numerical experiments demonstrate that the proposed mixed- (single/half-) precision algorithms are up to 60 times faster than their double precision equivalent while being orders of magnitude more accurate than their fully half-precision counterparts.

Keywords: Mixed precision, finite element method, finite element kernel and assembly, rounding error analysis, hardware acceleration, matrix units, Intel AMX.

1 Introduction

Hardware accelerators such as graphical processing units (GPUs) have been ubiquitously employed to accelerate finite element (FE) computations, leading to orders-of-magnitude speedups [7, 19, 24, 52, 59]. These improvements arise from the parallelization capabilities of GPUs and their efficiency at performing computations in reduced- and mixed-precision arithmetic. However, there is no comprehensive rounding error analysis of the FE method that can guide reduced-precision implementations and ensure their accuracy. In this paper we develop the first fine-grained rounding error analysis of FE cell kernels and assembly which includes mixed-precision implementations and hardware accelerators. This theory establishes the accuracy of mixed-precision hardware-accelerated FE kernels and assembly and can act as a guide for algorithmic design. Furthermore, we propose a strategy for mixed-precision hardware accelerated FE kernel implementations. We show that for high polynomial degrees these kernels are not just faster than double precision kernels, but are also orders of magnitude more accurate than their reduced-precision equivalent. Therefore, this work is a stepping stone towards comprehensive reduced-/mixed-precision FE implementations and their complete rounding error analysis.

Artificial intelligence and machine learning applications have been driving the development of computer chips that are particularly efficient at performing reduced- and mixed-precision computations¹. The list includes GPUs, tensor/intelligence/neural processing units (TPUs/IPUs/NPUs), field-programmable gate arrays (FPGAs), and others. Key components of these chips are matrix multiplication units² which perform fused-matrix-multiply-add instructions in reduced- or mixed-precision with a higher computational throughput than standard (e.g., vectorized) operations. For instance, NVIDIA H100 GPU half-precision tensor cores are over 32 times faster than standard double precision computations³. However, these chips are specifically tailored to graphics and machine learning workloads and exploiting these accelerators in broader scientific computing applications is an active field of investigation [1, 32].

*BCAM, Basque Center for Applied Mathematics, Bilbao, Spain & Ikerbasque, Basque Foundation for Science, Bilbao, Spain Email: mcroci@bcamath.org.

†Department of Engineering, University of Cambridge, UK. Email: gnw20@cam.ac.uk.

¹Parallelization is also an important aspect, but it is not the focus of this work.

²The naming convention of accelerators and matrix units is not standardized and dictated by marketing choices. For instance, we have tensor cores (NVIDIA), matrix cores (AMD), matrix multiply units (Google TPUs), advanced matrix extensions units (Intel), etc.

³See <https://developer.nvidia.com/blog/nvidia-hopper-architecture-in-depth/>.

Hardware-accelerated reduced- and mixed-precision scientific computing poses two challenges: 1) Computational bottlenecks must be offloaded, if possible, onto matrix-matrix multiplications (which are relatively inexpensive). 2) Rounding errors must be kept under control to ensure the accuracy of computations. Algorithmic advances thus require both a careful implementation and a thorough rounding error analysis.

The advantages of accelerating matrix-matrix multiplications via reduced- and mixed-precision matrix multiplication units have been widely investigated in the numerical linear algebra literature [1, 11, 20, 21, 28, 32, 42, 43]. However, these implementation strategies have not been fully incorporated within FE computations. Indeed, multiple studies [4, 7, 9, 14, 19, 24, 41, 50, 52, 53, 59] (the reference lists are in no way exhaustive) have presented GPU-accelerated FE algorithms, but these mainly exploit GPUs for parallelization and focus less on rounding error implications. For instance, the cited FE works do not employ half-precision floating-point arithmetic and do not mention tensor cores⁴.

Similarly, the rounding error analysis of the FE method is limited. Most of the available studies [2, 5, 23, 44] exclusively focus on rounding errors arising from the linear solver and from the conditioning of FE linear systems. The only exceptions are two studies ([60] and Section 8.5 in [18]) that focus on timestepping for parabolic problems and two more by Melosh and collaborators which analyze rounding errors in one of the first instances of the FE method: the FE analysis of structures [46, 47]. There is no existing work on any other component of the FE method, including FE kernels and assembly. Therefore, it is theoretically unclear whether FE computations in reduced- and mixed-precision can attain enough accuracy for practical purposes. On the other hand, there is a wide breadth of work on reduced- and mixed-precision numerical linear algebra algorithms (see [1, 32] and the references therein) as well as multiple studies on reduced-/mixed-precision timestepping [6, 12, 16, 17, 27, 40] and Newton’s method [38, 58]. These results, together with classical rounding error theory [29, 62], can be used as building blocks to derive a comprehensive rounding error analysis of the FE method. Such an analysis can then guide reduced- and mixed-precision hardware-accelerated implementations and the design of mixed-precision iterative solvers and related preconditioning strategies.

In this paper we take the first step in this direction by developing a fine-grained rounding error analysis of reduced- and mixed-precision FE cell kernels and assembly. In particular, we make the following new contributions:

- We derive the first rounding error analysis of FE kernels and assembly. This theory includes basis function tabulation, geometry computations, FE function and coefficient evaluations, and the evaluation of quadrature rules. Furthermore, it accounts for mixed-precision implementations and mixed-precision hardware accelerators, thus providing theoretical guidance for designing reduced- and mixed-precision FE algorithms. For the sake of brevity, the analysis is presented for Lagrange FE and mass and Poisson forms (both bilinear forms and actions) on simplices and boxed-cells (e.g., hexahedra), but should qualitatively apply to more general settings.
- We present a new mixed-precision FE kernel implementation strategy which employs: a) higher precision for geometry computations and FE tabulation, b) lower precision for storage, and c) mixed-precision for FE function evaluations and for summing together quadrature node contributions. We prove that these kernels are accurate to the machine precision of the lower precision format with a small error constant that is independent to leading order from: the conditioning of FE basis function evaluations, the ill-posedness of the cell, the polynomial degree, and the number of quadrature nodes. Conversely, we prove that the error constant is not independent from these quantities in fully reduced-precision implementations.
- We provide the first hardware-accelerated FE kernel implementations using mixed-precision fp32/bf16 Intel advanced matrix extension (AMX) units on Intel CPUs. For high-degree polynomials, AMX acceleration leads to a speedup factor of up to 60× with respect to double-precision vectorized computations for mass forms and up to 15× for Poisson forms. In contrast, we show that vectorized reduced- (fp16) and mixed- (fp32/bf16) precision kernels are never more than 4-6 times faster than double precision. Numerical results on a single CPU core support our rounding error analysis and thus provenly demonstrate that for high-degree polynomials mixed-precision hardware-accelerated kernels are faster than double precision kernels and orders of magnitude more accurate than their corresponding low-precision implementations. These results also show that it is possible to evaluate FE kernels robustly at half-precision accuracy.
- As a side theoretical contribution, we provide the first rounding error analysis of the evaluation of multivariate Lagrange polynomials and their gradients on simplices (and boxed cells). The analysis shows that multivariate Lagrange polynomials and their derivatives can be evaluated to high absolute and relative (absolute only for

⁴Some references [9, 41, 52, 59] mention or use cuBLAS which, among other functionalities, implements tensor-core-accelerated matrix-matrix multiplications. It is not stated in these papers whether these features have been exploited.

derivatives) pointwise accuracy. We highlight that the rounding error analysis of the evaluation of 1D Lagrange polynomials and generic multivariate polynomials is well-known (cf. [30] and [51] respectively).

We remark that while our rounding error analysis and implementation strategies are not specific to a given set of floating-point formats, matrix multiplication units often employ half precision which may limit the ultimate accuracy of the FE method. However, this is not necessarily problematic: Often in computational sciences and engineering a few digits of accuracy is all is needed. Furthermore, half-precision-accurate FE kernels and assembly can still accelerate computations in applications that warrant higher accuracy. Indeed, there is a wide range of mixed-precision techniques which obtain high-precision accuracy at low-precision costs by exploiting fast reduced-precision accurate computations. The list includes: mixed-precision iterative refinement methods [3, 13, 28, 49], mixed-precision Newton [38, 58], mixed-precision multigrid [45, 57], and mixed-precision iterative solvers and preconditioning strategies [1, 13, 22, 25]. We leave the investigation of how these techniques can be combined with mixed-precision FE kernels and assembly to future work.

The paper is structured as follows: Section 2 contains a brief introduction to rounding error analysis and hardware accelerators. In Section 3 we introduce the forms, cell kernels, and assembly algorithms we consider in the paper. In Section 4 we develop a comprehensive rounding error analysis of these algorithms which accounts for mixed-precision implementations and hardware accelerators. Numerical results supporting the theory are presented in Section 5. Finally, Section 6 contains our concluding remarks.

2 Background

We begin this section by describing the notation adopted throughout the paper. Then, we provide an introduction to rounding error analysis and to the theoretical results from numerical linear algebra to be used as building blocks for the theory developed in Section 4. Finally, we provide some background on mixed-precision hardware accelerators in Section 2.3.

2.1 Notation

In this paper, we adopt the following notation:

- **Constants.** For simplicity of notation we indicate with c a generic constant and we use numbers to denote different constants appearing in the same equation, e.g., c_1 , c_2 , etc. Constants with the same name appearing in different equations do not necessarily share the same value. We use $a \lesssim b$ to indicate that $a \leq cb$ for a constant $c > 0$. We indicate dimension-dependent constants with $c(d)$.
- **Scalars, vectors, matrices, and tensor.** We indicate scalars with lower-case letters (e.g., a , b , etc.), column vectors with lower-case bold letters (e.g., \mathbf{a} , \mathbf{b} , etc.), and matrices and tensors with capitals. The only exception to this rule is for variables which are of higher tensor order in the Poisson kernels than in the mass kernels. In this case we use the higher tensor order notation for both for simplicity (e.g., if a variable is a matrix for Poisson and a vector for the mass form we use an upper case letter). We employ the following partial indexing notation for tensors: if, e.g., $A \in \mathbb{R}^{m \times n \times q \times r}$ is a fourth-order tensor, we indicate with $A_i \in \mathbb{R}^{n \times q \times r}$ and $A_{ij} \in \mathbb{R}^{q \times r}$ respectively the third- and second-order tensors obtained after fixing the first dimensions.
- **Linear algebra.** For a matrix A or a column vector \mathbf{b} we indicate with A^T and \mathbf{b}^T their transposes and with $\|A\|_p$ and $\|\mathbf{b}\|_p$ their p norm respectively. For a set $\{A^k\}_{k=1}^n$ of square matrices we indicate with $\text{diag}_{k=1}^n(A^k)$ the block diagonal matrix whose k -th block is given by A^k . For a set $\{\mathbf{v}^k\}_{k=1}^n$ of column vectors we denote with $\text{vstack}_{k=1}^n(\mathbf{v}^k)$ the column vector obtained by vertically stacking the column vectors. For a set of scalars $\{a_k\}_{k=1}^n$ we indicate with $[a_k]_{k=1}^n$ the column vector \mathbf{a} such that its k -th entry is given by a_k .
- **Rounding errors.** We denote with u a unit roundoff and we possibly use subscripts to distinguish between the units roundoff of different precisions and floating-point formats (cf. Table 1). We indicate with δ single roundoffs which satisfy $|\delta| \leq u$. We denote with θ_n generic $O(nu)$ rounding error terms which we define in Lemma 2.1. Different θ_n terms need not have the same value, but all θ_n terms are bounded by $|\theta_n| \leq \gamma_n \leq cu$ (also defined in Lemma 2.1). We will use superscripts to denote δ , θ_n , γ_n terms which arise from calculations performed in different precisions. Finally, for any quantity a we indicate with \hat{a} the result of its finite-precision computation and with Δa we denote the corresponding rounding error: $\Delta a := \hat{a} - a$.
- **Condition numbers.** We denote condition numbers of numerical computations with the Greek letter κ . Additionally, for a square matrix A , we indicate with $\kappa_p(A)$ the p -norm condition number of A .

Format	u	x_{\min}	x_{\max}	t	exponent bits
bf16/bfloat16 (half)	3.91×10^{-3}	1.18×10^{-38}	3.39×10^{38}	8	8
fp16 (half)	4.88×10^{-4}	6.10×10^{-5}	6.55×10^4	11	5
fp32 (single)	5.96×10^{-8}	1.18×10^{-38}	3.40×10^{38}	24	8
fp64 (double)	1.11×10^{-16}	2.22×10^{-308}	1.80×10^{308}	53	11

Table 1: Overview of commonly used floating point systems. Here $u = 2^{-t}$ is the roundoff unit, x_{\min} in the smallest normalized positive number, x_{\max} is the largest finite number and t is the precision. While *bf16* and *fp32* have the same range and exponent bits, *fp16* has a smaller roundoff unit (higher precision) at the cost of a smaller range.

- **Domain and mesh.** Let $D \subset \mathbb{R}^d$ be an open polyhedral domain in \mathbb{R}^d . For any such D , we denote with D_h a non-degenerate tessellation of D made of either simplices or boxed cells (e.g., quadrilaterals or hexahedra). We denote with $K \in D_h$ a cell of D_h and with \tilde{K} the reference cell.

2.2 Background on rounding error analysis

There are multiple floating-point number formats available. In this paper we only use four, which are listed in Table 1 together with their properties. We start by giving some basic definitions:

Definition 2.1. The terms *reduced precision* and *low precision* denote the use of floating-point number formats with larger unit roundoffs (e.g., *fp16* or *bf16*), in contrast to *high precision* formats which are more accurate (e.g., *fp32* or *fp64*).

Definition 2.2. *Reduced- and high-precision algorithms* are algorithms which are run entirely in the same precision (low or high respectively) as opposed to *mixed-precision algorithms* that employ different formats. Typically a mixed-precision algorithm employs both high- and low-precision computations.

Next, we describe the standard floating point error model which applies to round-to-nearest computations (cf. Chapter 2 of [29]):

$$\widehat{(a \text{ op } b)} = (a \text{ op } b)(1 + \delta), \quad |\delta| < u, \quad \text{op} \in \{+, -, \times, \backslash\}. \quad (1)$$

Here u is the roundoff unit and δ is called a roundoff error. In the above and throughout the paper we use hats to denote quantities that are the result of finite precision computations. By using the model in (1) it is possible to derive *a priori* rounding error bounds for a variety of different algorithms and operations [29].

Products and ratios of multiple $(1 + \delta)$ terms often arise in rounding error analysis. It is thus advantageous to simplify the notation by invoking the following result:

Lemma 2.1 (Lemma 3.1 in [29]). *If $|\delta_i| \leq u$ and $\rho_i = \pm 1$ for $i = 1, \dots, n$ and $nu < 1$, then*

$$\prod_{i=1}^n (1 + \delta_i)^{\rho_i} = (1 + \theta_n), \quad \text{where} \quad |\theta_n| \leq \frac{nu}{1 - nu} := \gamma_n. \quad (2)$$

If u is sufficiently small, then there exists $c \geq 1$ such that $\gamma_n \leq cu$.

We will use the θ_n and γ_n notations throughout the paper. We remark that θ_n indicates a generic error term and two θ_n terms need not be the same value unless they arise from exactly the same computation. Nevertheless, all error terms indicated with θ_n are always bounded in absolute value by γ_n . Manipulation of multiple θ_n and γ_n terms is made easier thanks to the following lemma:

Lemma 2.2 (Lemma 3.3 in [29]). *For any positive integer k let θ_k denote a quantity bounded according to $|\theta_k| \leq \gamma_k = ku/(1 - ku)$. The following relations hold:*

$$(1 + \theta_k)(1 + \theta_j) = 1 + \theta_{k+j}, \quad i\gamma_k \leq \gamma_{ik}, \quad \gamma_k + u \leq \gamma_{k+1}, \quad \gamma_k + \gamma_j + \gamma_k\gamma_j \leq \gamma_{k+j}.$$

In this paper we will make use of the above relations without explicitly referring to this lemma. We will also make use of a series of results of classical rounding error analysis related to inner products, matrix-vector and matrix-matrix products, matrix inversion, and determinant computations.

a) Inner products. The following backward error result holds for the inner products between two vectors (see equation (3.4) in [29]): Let $\mathbf{a}, \mathbf{b} \in \mathbb{R}^n$, then,

$$\widehat{\mathbf{a}^T \mathbf{b}} = (\mathbf{a} + \Delta \mathbf{a})^T \mathbf{b}, \quad \text{where } |\Delta \mathbf{a}| \leq \gamma_n |\mathbf{a}| \leq cnu |\mathbf{a}|, \quad (3)$$

where the bound is to be interpreted entrywise. The above bound implies that an inner product computed in finite-precision arithmetic is equivalent to an exact inner product between perturbed vectors.

b) Matrix-vector products. The following backward error result holds for matrix-vector products (see equation (3.11) in [29]): Let $A \in \mathbb{R}^{m \times n}$, $\mathbf{b} \in \mathbb{R}^n$, then,

$$\widehat{A\mathbf{b}} = (A + \Delta A)\mathbf{b}, \quad \text{where } |\Delta A| \leq \gamma_n |A| \leq cnu |A|, \quad (4)$$

where the bound is to be interpreted entrywise. The above bound implies that a matrix-vector product computed in finite-precision arithmetic is equivalent to an exact matrix-vector product with a perturbed matrix.

c) Matrix-matrix products. The following forward error result holds for matrix-vector products (see equation (3.13) in [29]): Let $A \in \mathbb{R}^{m \times n}$, $B \in \mathbb{R}^{n \times l}$, $C = AB$, then,

$$\widehat{C} = C + \Delta C, \quad \text{where } |\Delta C| \leq \gamma_n |A| |B| \leq cnu |A| |B|. \quad (5)$$

Again, the bound is to be interpreted entrywise.

d) Matrix inversion. Another result which we will be using is a forward error bound for computing the inverse of a matrix $A \in \mathbb{R}^{n \times n}$. Since there are many algorithms for matrix inversion available (cf. [29]) we assume that the one we use satisfies the following assumption (see equation (14.3) in [29]):

Assumption 2.1. The matrix inversion algorithm yields an approximation $\widehat{A^{-1}} \approx A^{-1}$ which satisfies

$$|\widehat{A^{-1}} - A^{-1}| \leq c(n)u |A^{-1}| |A| |A^{-1}|, \quad (6)$$

for a positive constant $c(n)$ which grows with n .

e) Determinant computation. The following theorems describe how rounding errors affect the computation of determinants computed through an LU factorization (e.g., this is what LAPACK does).

Theorem 2.3 (Theorem 9.3, Section 9, and Section 14.6 in [29]). *The LU factorization of a matrix $A \in \mathbb{R}^{n \times n}$ yields LU factors \hat{L} and \hat{U} satisfying*

$$\hat{L}\hat{U} = A + \Delta A, \quad \text{where } |\Delta A| \leq c(n)u |\hat{L}| |\hat{U}|, \quad (7)$$

where $c(n)$ is a constant growing with n . Assuming that no underflow/overflow occurs⁵, computing the determinant as $\det(\hat{U})$ yields

$$\widehat{\det(A)} = \det(\hat{U})(1 + \theta_n), \quad \text{where } |\theta_n| \leq cnu. \quad (8)$$

Since $\det(\hat{U}) = \det(A + \Delta A)$, this means that in finite precision we compute the (almost) exact determinant of a slightly perturbed matrix. To obtain a final bound for the error, we invoke the following perturbation result for determinants:

Theorem 2.4 (Corollary 2.14 in [35]). *If $A \in \mathbb{R}^{n \times n}$ is non-singular, then it holds that*

$$|\det(A + E) - \det(A)| \leq \left((\|A^{-1}\|_2 \|E\|_2 + 1)^n - 1 \right) |\det(A)| \leq cn \|A^{-1}\|_2 \|E\|_2 |\det(A)|. \quad (9)$$

Corollary 2.5. *Let $A \in \mathbb{R}^{n \times n}$ be non-singular and assume that u is sufficiently small. If $\det(A)$ is computed via the LU factorization of A and no underflows/overflows occur, then it holds*

$$|\widehat{\det(A)} - \det(A)| \leq c(n)u \kappa_2(A) |\det(A)|, \quad (10)$$

where $\kappa_2(A)$ is the 2-norm condition number of A and $c(n)$ is a positive constant growing with n .

⁵For determinants in particular, this is a strong assumption, although there are remedies: see Section 14.6 in [29].

Proof. The proof is obtained by setting $E = \Delta A$ in Theorem 2.4 and applying Theorem 2.3 to bound the perturbation together with the bound $\|\hat{L}\|\hat{U}\|_2 \leq c(n)\|A\|_2$ which is a consequence of [29, Lemma 9.6]. \square

We will use all the above results as building blocks for deriving rounding error bounds for the whole assembly process.

Remark 2.1. All the above bounds (and thus the bounds derived in the next pages) are worst-case rounding error bounds. We remark that rounding errors may be more lenient in practice: they often behave as independent random variables leading to smaller error growth rates with respect to n due to stochastic error cancellations [31]. Under this scenario all the bounds listed here would still hold after replacing γ_n with the smaller $\tilde{\gamma}_n = O(n^{1/2})$. However, it is difficult to predict *a priori* whether this will happen for a given calculation.

2.3 Background on mixed-precision hardware accelerators

Mixed-precision hardware accelerators are specialized units which perform multiply-add operations with superior performance. They are typically present in GPUs as well as in chips tailored to artificial intelligence and machine learning workloads. Intel Xeon 4th-generation scalable processors also include mixed-precision hardware accelerators.

In this paper we aim to exploit these hardware capabilities to either accelerate FE kernels (and therefore assembly) and/or to increase their accuracy when reduced-precision formats are employed. There are two types of accelerators which are relevant to our work: 1) Mixed-precision vector units, performing entrywise multiply-add operations between vectors. 2) Mixed-precision matrix units, performing fused-matrix-multiply-add operations. In both cases the input arrays are stored in a lower-precision format (e.g., fp16 or bf16) and the multiply-add operation is performed in a higher precision format (e.g., fp32), which is also used for storing the result. The maximum array size is restricted by the size of the accelerator registers and the multiplication between larger arrays must necessarily be blocked.

Although our rounding error analysis is independent from the accelerator or chip used, we only consider CPU implementations in our numerical experiments (cf. Section 5). Therefore, we only describe the properties of Intel CPU accelerators in detail here. Intel vector accelerators are called “advanced vector extensions” (AVX) units and Intel matrix accelerators are called “advanced matrix extensions” (AMX) units.

AVX units. AVX is the name used to denote vector accelerators in general, i.e., it also includes units which operate in the same precision and operations which are not necessarily entrywise vector-multiply-adds (for a full list, see the Intel Intrinsics Guide [34]). AVX units perform computations on vector registers of different sizes (up to 512 bits on AVX512 units). In particular, in this work we will use AVX512 operations when working in double, single, or fp16 half precision. For mixed-precision computations we will employ the AVX512-bf16 unit which performs a product between two bf16 vectors of 32 entries (i.e., 512 bits), adds the result to a single precision vector of 16 entries (again 512 bits), and accumulates it into another single precision vector of the same size. Namely, given the vectors

$$\mathbf{a} = [a_1, \dots, a_{32}]^T, \quad \mathbf{b} = [b_1, \dots, b_{32}]^T, \quad \mathbf{c} = [c_1, \dots, c_{16}]^T, \quad (11)$$

with \mathbf{a}, \mathbf{b} stored contiguously in bf16 and \mathbf{c} stored contiguously in single precision, the AVX512-bf16 unit computes

$$\mathbf{c} += \tilde{\mathbf{a}}^1 \circ \tilde{\mathbf{b}}^1 + \tilde{\mathbf{a}}^2 \circ \tilde{\mathbf{b}}^2, \quad (12)$$

where \circ denotes the entrywise vector product and all operations are performed in single precision [34]. The vectors $\tilde{\mathbf{a}}$ and $\tilde{\mathbf{b}}$, of length 16, are given by

$$\tilde{\mathbf{a}}^1 = [a_1, a_3, \dots, a_{31}]^T, \quad \tilde{\mathbf{a}}^2 = [a_2, a_4, \dots, a_{32}]^T, \quad \tilde{\mathbf{b}}^1 = [b_1, b_3, \dots, b_{31}]^T, \quad \tilde{\mathbf{b}}^2 = [b_2, b_4, \dots, b_{32}]^T. \quad (13)$$

AVX512-bf16 fused-multiply-add instructions perform 64 floating-point operations per cycle which is 4 times more than AVX512 fused-multiply-add double precision units and the same as AVX512 fused-multiply-add fp16 half-precision instructions. Therefore, implementations exploiting these mixed-precision accelerators can be up to 4 times faster than double precision and as fast as half-precision computations (albeit being more accurate than pure half-precision operations).

AMX units. AMX is the name used by Intel to denote matrix accelerators. The Intel Intrinsic Guide [34] includes only load and store operations into matrix registers as well as fused-matrix-multiply-add operations. Here we are only concerned with the mixed-precision fp32/bf16 instructions in the AMX-bf16 extension set [34]. These instructions work with matrices of variable sizes. Here we use the largest matrix size which fits the AMX registers: 16 rows of 64 bits each, corresponding to 16-by-16 for single precision matrices and 16-by-32 for bf16 matrices (better seen as two packed 16-by-16 bf16 matrices, see next). The AMX-bf16 mixed-precision matrix multiplication units work as follows: given the contiguously-stored matrices

$$A = \begin{bmatrix} a_{1,1} & a_{1,2} & \cdots & a_{1,32} \\ a_{2,1} & a_{2,2} & \cdots & a_{2,32} \\ \cdots & \cdots & \cdots & \cdots \\ a_{16,1} & a_{16,2} & \cdots & a_{16,32} \end{bmatrix}, \quad B = \begin{bmatrix} b_{1,1} & b_{1,2} & \cdots & b_{1,32} \\ b_{2,1} & b_{2,2} & \cdots & b_{2,32} \\ \cdots & \cdots & \cdots & \cdots \\ b_{16,1} & b_{16,2} & \cdots & b_{16,32} \end{bmatrix}, \quad C = \begin{bmatrix} c_{1,1} & c_{1,2} & \cdots & c_{1,16} \\ c_{2,1} & c_{2,2} & \cdots & c_{2,16} \\ \cdots & \cdots & \cdots & \cdots \\ c_{16,1} & c_{16,2} & \cdots & c_{16,16} \end{bmatrix},$$

where $A, B \in \mathbb{R}^{16 \times 32}$ are stored in bf16 and $C \in \mathbb{R}^{16 \times 16}$ in single precision, the AMX units compute

$$C += \tilde{A}_1 \tilde{B}_1 + \tilde{A}_2 \tilde{B}_2, \quad (14)$$

where all operations are performed in single precision by flushing output subnormals to zero [33] and \tilde{A}_1, \tilde{A}_2 are given by

$$\tilde{A}_1 = \begin{bmatrix} a_{1,1} & a_{1,3} & \cdots & a_{1,31} \\ a_{2,1} & a_{2,3} & \cdots & a_{2,31} \\ \cdots & \cdots & \cdots & \cdots \\ a_{16,1} & a_{16,3} & \cdots & a_{16,31} \end{bmatrix}, \quad \tilde{A}_2 = \begin{bmatrix} a_{1,2} & a_{1,4} & \cdots & a_{1,32} \\ a_{2,2} & a_{2,4} & \cdots & a_{2,32} \\ \cdots & \cdots & \cdots & \cdots \\ a_{16,2} & a_{16,4} & \cdots & a_{16,32} \end{bmatrix}, \quad (15)$$

i.e., \tilde{A}_1 and \tilde{A}_2 are the submatrices of A respectively containing its odd and even columns. \tilde{B}_1 and \tilde{B}_2 are defined in the same way.

We remark that when the matrices that need to be multiplied are larger than what fits in the AMX registers the matrix multiplication must be decomposed into smaller matrix-multiply-add operations like (14). It is also worth mentioning that this decomposition often involves a non-trivial memory reorganization of the inputs.

Example 2.1. We clarify this issue with an example: let us assume for simplicity that the input bf16 sizes were 3-by-6 rather than 16-by-32 and that we wanted to compute a matrix product AB between two matrices A and B of size 3-by-12 and 12-by-3 respectively. Let A be stored contiguously as

$$A = \left[\begin{array}{ccc|ccc|ccc|ccc} a_{1,1} & a_{1,2} & a_{1,3} & a_{1,4} & a_{1,5} & a_{1,6} & a_{1,7} & a_{1,8} & a_{1,9} & a_{1,10} & a_{1,11} & a_{1,12} \\ a_{2,1} & a_{2,2} & a_{2,3} & a_{2,4} & a_{2,5} & a_{2,6} & a_{2,7} & a_{2,8} & a_{2,9} & a_{2,10} & a_{2,11} & a_{2,12} \\ a_{3,1} & a_{3,2} & a_{3,3} & a_{3,4} & a_{3,5} & a_{3,6} & a_{3,7} & a_{3,8} & a_{3,9} & a_{3,10} & a_{3,11} & a_{3,12} \end{array} \right]. \quad (16)$$

In order to compute the product, A would need to first be reorganized⁶ contiguously in memory as

$$A = \left[\begin{array}{cc|ccc} \tilde{A}_{1,1} & \tilde{A}_{1,2} & & & & \\ \tilde{A}_{2,1} & \tilde{A}_{2,2} & & & & \\ & & a_{1,4} & a_{1,5} & a_{1,6} & \\ & & a_{2,4} & a_{2,5} & a_{2,6} & \\ & & a_{3,4} & a_{3,5} & a_{3,6} & \\ & & a_{1,7} & a_{1,10} & a_{1,8} & \\ & & a_{2,7} & a_{2,10} & a_{2,8} & \\ & & a_{3,7} & a_{3,10} & a_{3,8} & \end{array} \right] = \left[\begin{array}{ccc|ccc} a_{1,1} & a_{1,4} & a_{1,2} & a_{1,5} & a_{1,3} & a_{1,6} \\ a_{2,1} & a_{2,4} & a_{2,2} & a_{2,5} & a_{2,3} & a_{2,6} \\ a_{3,1} & a_{3,4} & a_{3,2} & a_{3,5} & a_{3,3} & a_{3,6} \\ \hline a_{1,7} & a_{1,10} & a_{1,8} & a_{1,11} & a_{1,9} & a_{1,12} \\ a_{2,7} & a_{2,10} & a_{2,8} & a_{2,11} & a_{2,9} & a_{2,12} \\ a_{3,7} & a_{3,10} & a_{3,8} & a_{3,11} & a_{3,9} & a_{3,12} \end{array} \right]. \quad (17)$$

Only after rearranging A and performing a similar, albeit different, rearranging of B (which we omit for brevity) one can finally compute AB as follows: First, let $C \in \mathbb{R}^{3 \times 3}$ be the zero matrix stored in single precision. Second, use AMX units twice (loading the entries of A and B in two batches of 18 numbers each) to compute

$$C += \tilde{A}_{1,1} \tilde{B}_{1,1} + \tilde{A}_{1,2} \tilde{B}_{1,2}, \quad (18)$$

$$C += \tilde{A}_{2,1} \tilde{B}_{2,1} + \tilde{A}_{2,2} \tilde{B}_{2,2}. \quad (19)$$

The resulting C is then equal to AB .

⁶The reshaping is only for the sake of explanation: what is important here is that each row is stored contiguously one after the other.

The appeal of using AMX cores lies in their efficiency: They perform 1024 floating-point operations per cycle [33] which are 64 times more than AVX512 fused-multiply-add double precision instructions. Therefore, codes exploiting AMX-bf16 instructions can in principle be up to 64 times faster than their double precision equivalents. Of course this is just a theoretical upper bound: this speedup is only obtainable on fused-matrix-multiply-add operations of the form (14) and not on any other computation. Nevertheless, these considerations provide a recipe for making full use of AMX accelerators: large speedups are obtainable if algorithms are implemented so that their computational bottleneck is comprised of matrix-matrix products or fused-matrix-multiply-add operations. This is exactly what motivates the FE kernel implementations presented in the next section.

3 Local kernel algorithm and global assembly

In this section we introduce the FE kernels we consider in the paper. First, we describe the FE forms and then we present the kernel algorithms. For the latter we select an implementation in which matrix-matrix products are the bottleneck in order to exploit AMX accelerators. Finally, we briefly mention the assembly process which is the direct application of our work.

Since rounding error analyses are specific to the actual computations performed, covering the whole set of possible FE forms and elements would unnecessarily complicate and lengthen the exposition. Therefore, we adopt the following simplifications:

1. We only consider the mass and Poisson linear (actions) and bilinear (matrix) forms (with coefficients).
2. We only work with Lagrange elements on simplices and boxed cells (e.g., quadrilaterals and hexahedra).
3. We assume that all FE basis functions appearing in the forms belong to the same FE approximation subspace.

We expect the generalization of our results to other forms and elements to yield qualitatively similar results.

3.1 Cell kernels

Let D be an open domain with compact closure in \mathbb{R}^d and let D_h be a tessellation of D comprised of simplices or boxed cells. The mass and Poisson forms over a single cell $K \in D_h$ read:

$$a_K(w, v) = \int_K z(\mathbf{x}) w v \, d\mathbf{x}, \quad (\text{mass form}), \quad a_K(w, v) = \int_K z(\mathbf{x}) \nabla w \cdot \nabla v \, d\mathbf{x}, \quad (\text{Poisson form}), \quad (20)$$

where w, v , and z all belong to the same FE approximation space. We directly consider the evaluation of the forms over the reference cell and take $\Phi = [\phi_k]_{k=1}^{n_\phi}$ to be the reference basis functions. We consider the computation of

$$A_{ji} = a_{\tilde{K}}(\phi_i, \phi_j), \quad v_j = a_{\tilde{K}}(w, \phi_j), \quad (21)$$

where w is now a known function and $a_{\tilde{K}}$ is the bilinear form over K mapped onto the reference cell \tilde{K} . Here $A \in \mathbb{R}^{n_\phi \times n_\phi}$ and $\mathbf{v} \in \mathbb{R}^{n_\phi}$ are the (local) matrix and vector that encode the bilinear and linear form over K respectively.

After mapping the mass form to the reference cell we obtain

$$A = \int_{\tilde{K}} \tilde{z}(\tilde{\mathbf{x}}) |\det(J(\tilde{\mathbf{x}}))| (\Phi(\tilde{\mathbf{x}}) \otimes \Phi(\tilde{\mathbf{x}})) \, d\tilde{\mathbf{x}}, \quad \mathbf{v} = \int_{\tilde{K}} (\tilde{z}(\tilde{\mathbf{x}}) |\det(J(\tilde{\mathbf{x}}))| \tilde{w}(\tilde{\mathbf{x}})) \Phi(\tilde{\mathbf{x}}) \, d\tilde{\mathbf{x}}. \quad (22)$$

Here $\tilde{z}(\tilde{\mathbf{x}})$ and $\tilde{w}(\tilde{\mathbf{x}})$ are the result of mapping the functions z and w onto the reference cell and $|\det(J(\tilde{\mathbf{x}}))|$ is the absolute value of the determinant of the Jacobian $J(\tilde{\mathbf{x}})$ of the reference map. For the Poisson forms we instead obtain

$$A = \sum_{s=1}^d \sum_{t=1}^d \bar{A}_{st}, \quad \mathbf{v} = \sum_{s=1}^d \bar{\mathbf{v}}_s, \quad (23)$$

where $\bar{A} \in \mathbb{R}^{d \times d \times n_\phi \times n_\phi}$, $\bar{\mathbf{v}}_s \in \mathbb{R}^{n_\phi}$ are defined as follows: for $s = 1, \dots, d$, $t = 1, \dots, d$,

$$\bar{A}_{st} = \int_{\tilde{K}} \check{C}_{st}(\tilde{\mathbf{x}}) (\partial_{\tilde{\mathbf{x}}_t} \Phi(\tilde{\mathbf{x}}) \otimes \partial_{\tilde{\mathbf{x}}_s} \Phi(\tilde{\mathbf{x}})) \, d\tilde{\mathbf{x}}, \quad \bar{\mathbf{v}}_s = \int_{\tilde{K}} \check{r}_s(\tilde{\mathbf{x}}) \partial_{\tilde{\mathbf{x}}_s} \Phi(\tilde{\mathbf{x}}) \, d\tilde{\mathbf{x}}. \quad (24)$$

Here, $\check{C}(\check{\mathbf{x}}) \in \mathbb{R}^{d \times d}$ and $\check{\mathbf{r}}(\check{\mathbf{x}}) \in \mathbb{R}^d$ are given by

$$C(\check{\mathbf{x}}) = \check{z}(\check{\mathbf{x}})G(\check{\mathbf{x}}), \quad \check{\mathbf{r}}(\check{\mathbf{x}}) = \check{z}(\check{\mathbf{x}})(G(\check{\mathbf{x}})\nabla\check{w}(\check{\mathbf{x}})), \quad (25)$$

$$\text{where } G(\check{\mathbf{x}}) = |\det(J(\check{\mathbf{x}}))|(J^{-1}(\check{\mathbf{x}}))(J^{-1}(\check{\mathbf{x}}))^T \in \mathbb{R}^{d \times d} \quad (26)$$

is the geometry tensor. We highlight the fact that the functions $\check{C}(\check{\mathbf{x}})$ and $\check{\mathbf{r}}(\check{\mathbf{x}})$ incorporate both geometry and form coefficient information.

Note that the mass form can also be written in a similar way by setting $G(\check{\mathbf{x}}) = |\det(J(\check{\mathbf{x}}))|$, $\check{\mathbf{r}}(\check{\mathbf{x}}) = \check{z}(\check{\mathbf{x}})G(\check{\mathbf{x}})\check{w}(\check{\mathbf{x}})$, $\bar{\mathbf{v}}_1 = \mathbf{v}$, and $\bar{A}_{11} = A$. Therefore, for both forms we can write the local cell matrix and vector as

$$A = \sum_{s=1}^{n_d} \sum_{t=1}^{n_d} \bar{A}_{st}, \quad \mathbf{v} = \sum_{s=1}^{n_d} \bar{\mathbf{v}}_s, \quad (27)$$

where $n_d = d$ for Poisson and $n_d = 1$ for the mass form and $\bar{A} \in \mathbb{R}^{n_d \times n_d \times n_\phi \times n_\phi}$.

Remark 3.1. Most forms can be expressed as sums similar to (27) by considering each term in the sum to be the discretization of a monomial term comprised of integrals of derivatives of basis function components, cf. [39, 54].

After exactly integrating the integrals in (27) exactly⁷ with suitable quadrature rules $\{(\omega_q, \check{\mathbf{x}}_q)\}_{q=1}^{n_q}$ we can write each term in the sums as

$$\bar{A}_{st} = B_s C_{st} B_t^T, \quad \bar{\mathbf{v}}_s = B_s \mathbf{r}_s, \quad (28)$$

where C is a fourth-order sparse tensor such that

$$C_{st} = \text{diag}_q(\omega_q \check{C}_{st}(\check{\mathbf{x}}_q)) \in \mathbb{R}^{n_q \times n_q}, \quad (29)$$

$\mathbf{r}_s \in \mathbb{R}^{n_q}$ is given by

$$\mathbf{r}_s = \text{vstack}_q(\omega_q \check{\mathbf{r}}_s(\check{\mathbf{x}}_q)), \quad (30)$$

and $B \in \mathbb{R}^{n_d \times n_\phi \times n_q}$ is a third-order tensor with entries given by

$$B_{skq} = \partial_{\check{x}_s} \phi_k(\check{\mathbf{x}}_q), \quad B_{skq} = \phi_k(\check{\mathbf{x}}_q), \quad (31)$$

for the Poisson and the mass form respectively. Therefore, for both forms we can express A as the sum of n_d^2 triple matrix products:

$$A = \sum_{s=1}^{n_d} \sum_{t=1}^{n_d} B_s C_{st} B_t^T, \quad (32)$$

and \mathbf{v} as the sum of n_d matrix-vector products:

$$\mathbf{v} = \sum_{s=1}^{n_d} B_s \mathbf{r}_s. \quad (33)$$

The fact that A is expressed as a sum of matrix-matrix products leads to a kernel implementation that is amenable to AMX acceleration (as well as AVX). However, the same does not apply to \mathbf{v} , which only includes matrix-vector products and, as such, can only be accelerated with vector units. As a solution, we batch kernel computations by groups of n_{batch} cells (n_{batch} must be divisible by 16 to get the most out of AMX computations, cf. 2.3), thus obtaining

$$V^{\text{batch}} = \sum_{s=1}^{n_d} B_s R_s^{\text{batch}}, \quad \text{where } V^{\text{batch}} = [\mathbf{v}^1 | \dots | \mathbf{v}^{n_{\text{batch}}}], \quad R_s^{\text{batch}} = [\mathbf{r}_s^1 | \dots | \mathbf{r}_s^{n_{\text{batch}}}], \quad (34)$$

where V_s^{batch} and R_s^{batch} are matrices of size n -by- n_{batch} and n_q -by- n_{batch} respectively (recall that $B_s \in \mathbb{R}^{n \times n_q}$ only depends on the reference cell).

Remark 3.2. In what follows, we present our kernel algorithms and rounding error analysis without cell-batching for simplicity, but we do use cell-batching in our numerical experiments (cf. Section 5). Our theory applies to cell-batching as-is since the computation on each column of V^{batch} is performed independently.

We are now ready to describe the cell kernel algorithms used in this paper.

⁷We use exact quadrature for simplicity. Using inexact rules does not change our argument.

3.2 Local kernel algorithms

In this paper we consider the following local kernel algorithms. Both are amenable to AMX and AVX acceleration.

Algorithm 1. Local kernel algorithm for bilinear forms.

1. Tabulate the basis function values forming B .
2. Compute C .
3. Compute $H_{st} = C_{st}B_t^T$ for all $s, t \in \{1, \dots, n_d\}$.
4. Compute $A = \sum_{s=1}^{n_d} \sum_{t=1}^{n_d} B_s H_{st}$.

Remark 3.3. Another option is to compute $\tilde{H}_s = \sum_{t=1}^{n_d} H_{st}B_t^T$ so that $A = \sum_{s=1}^{n_d} B_s \tilde{H}_s$. This strategy leads to nearly the same rounding error analysis and error bounds.

Algorithm 2. Local kernel algorithm for linear forms.

1. Tabulate the basis function values forming B .
2. Compute \mathbf{r}_s for all s .
3. Compute $\mathbf{v} = \sum_{s=1}^{n_d} B_s \mathbf{r}_s$ (using cell batching).

Remark 3.4. For the sake of brevity, we only consider the above algorithms. We also do not analyze sum factorization approaches which are often used for tensor product FEs (see, e.g., [37, Section 4.1]). The adaptation of our rounding error analysis to different kernel implementations should hopefully be straightforward.

Once the local kernels have been run over all cells, every FE code assembles the resulting local tensors into a global tensor. This process, called assembly, is the natural application of faster FE kernels and is briefly described next.

3.3 Global Assembly

Assembly is the process through which the local matrices and vectors obtained from running the kernels are collected into a global tensor. Let n_K be the total number of cells and let n_g be the number of global degrees of freedom. Using linear algebra, we can write the assembled global matrix A^g and vector \mathbf{v}^g as

$$A^g = LDL^T, \quad \mathbf{v}^g = L\mathbf{b}, \quad (35)$$

where

$$D = \text{diag}_{k=1}^{n_K}(A^k), \quad \mathbf{b} = \text{vstack}_{k=1}^{n_K}(\mathbf{v}^k), \quad (36)$$

and A^k, \mathbf{v}^k are the local kernel matrix and vector on the k -th cell respectively. Here $L \in \{0, 1\}^{n_g \times n_\phi n_K}$ is a boolean assembly matrix with at most one non-zero per column that encodes the local-to-global map, see e.g., [61]. We take the evaluation of (35) as the assembly algorithm to be investigated in our rounding error analysis. For the sake of brevity, we do not consider the multitude of assembly algorithms available in the literature, but we remark that parallel implementations only change the order in which floating-point computations are performed and thus has no influence over the worst-case error analysis derived next.

4 Rounding error analysis

In this section we perform a comprehensive rounding error analysis of Algorithms 1 and 2 and of the assembly process. The analysis also includes mixed-precision implementations and accounts for hardware acceleration. That we are aware of this is the first rounding error analysis of FE kernels as well as the first rigorous result guiding the use of mixed-precision hardware accelerators in FE kernels.

Before we begin, we make two simplifying assumptions:

Assumption 4.1. We ignore floating point range effects, i.e., we assume underflow and overflow do not occur.

Assumption 4.2. We ignore rounding errors arising from mesh-generation and the computation of quadrature rules.

This latter assumption is sensible whenever the mesh and quadrature rules are computed in higher precision than the target accuracy of our computations. We remark that order-machine precision perturbations to mesh coordinates correspond to small relative perturbations of the mesh size and are thus unlikely to affect the overall FE approximation error provided that the mesh is of good enough quality.

We proceed in our analysis following the outline of Algorithms 1 and 2. We consider, in order, rounding errors arising from:

1. Basis function and finite element function evaluation (Section 4.1).
2. Geometry computations (Section 4.2).
3. Mixed-precision construction of the matrices and vectors appearing in Algorithms 1 and 2 (Section 4.3).
4. Mixed-precision accumulation of matrix-matrix products into A and v and global assembly (Section 4.4).

4.1 Finite element tabulation and function evaluation

Tabulating FE basis functions amounts to evaluating the reference basis functions and their derivatives, comprised of multivariate polynomials, at the quadrature nodes. Similarly, evaluating functions belonging to FE approximation subspaces consists of computing linear combinations of FE basis functions.

The rounding error analysis of univariate polynomials is classical (cf. Section 5 in [29]). The evaluation of univariate Lagrange polynomials has been analyzed by Higham in [30] and the multivariate version of Horner's algorithm has also been studied [51]. Nevertheless, there is no specific work on the evaluation of linear combinations of multivariate Lagrange polynomials and their derivatives. We present such an analysis in Appendix A. Here, we only describe the specific application of this analysis to Lagrange FE over simplices or boxed cells.

First, let $V_{\check{K}} = \text{span}(\Phi)$, where the entries of Φ form the degree- p nodal Lagrange reference basis over \check{K} . Also let $\partial_s V_{\check{K}} = \text{span}(\partial_s \Phi)$ and define the following condition numbers:

$$\kappa(V_{\check{K}}) := \max_{\check{\mathbf{x}} \in \check{K}} \|\Phi(\check{\mathbf{x}})\|_1, \quad \kappa(\partial_s V_{\check{K}}) := \max_{\check{\mathbf{x}} \in \check{K}} \|\partial_s \Phi(\check{\mathbf{x}})\|_1, \quad \text{and} \quad \kappa(\partial_s \Phi) := \max_{i=1, \dots, n_\phi} \kappa(\partial_s \phi_i). \quad (37)$$

Here $\kappa(V_{\check{K}})$ and $\kappa(\partial_s V_{\check{K}})$ are the condition numbers (also known as the Lebesgue constants) of the bases spanning $V_{\check{K}}$ and $\partial_s V_{\check{K}}$ respectively, while $\kappa(\partial_s \phi_i)$ is instead the condition number of the *evaluation* of the partial derivative of the i -th basis function (we refer to Lemma A.3 in Appendix A for the formal definition of $\kappa(\partial_s \phi_i)$).

Remark 4.1. The quantity $\kappa(V_{\check{K}})$ is the Lebesgue constant of the FE basis. It is well known that it can be made to grow polylogarithmically slow with the polynomial degree for boxed cells provided that the degrees of freedom are suitably chosen. On simplices the Lebesgue constant is larger, although it can be kept small even for moderately high-degree polynomials by constructing the FE basis accordingly, see e.g., [36].

We now state the following Lemma which provides rounding error bounds for the evaluation of FE functions and their derivatives:

Lemma 4.1. *Let \check{K} be a d -dimensional reference simplex or hypercube and let $V_{\check{K}} = \text{span}(\Phi)$, where the entries of Φ form the degree- p nodal Lagrange reference basis over \check{K} . Then, if u is sufficiently small, the evaluation of $\phi_i(\check{\mathbf{x}})$ and its derivatives in precision u satisfy, for all i and for all $\check{\mathbf{x}} \in \check{K}$, the bounds*

$$|\phi_i(\check{\mathbf{x}}) - \hat{\phi}_i(\check{\mathbf{x}})| \lesssim dpu |\phi_i(\check{\mathbf{x}})|, \quad (38)$$

$$\max_{\check{\mathbf{x}} \in \check{K}} |\partial_s \phi_i(\check{\mathbf{x}}) - \widehat{\partial_s \phi_i}(\check{\mathbf{x}})| \lesssim dpu \kappa(\partial_s \phi_i) \max_{\check{\mathbf{x}} \in \check{K}} |\partial_s \phi_i(\check{\mathbf{x}})|, \quad (39)$$

Furthermore, the evaluation of a function $z_h(\check{\mathbf{x}}) = \sum_{i=1}^{n_\phi} z_i \phi_i(\check{\mathbf{x}})$ and its derivatives satisfy the bounds

$$\max_{\check{\mathbf{x}} \in \check{K}} |z_h - \hat{z}_h| \lesssim p^d u \kappa(V_{\check{K}}) \|z\|_\infty, \quad (40)$$

$$\max_{\check{\mathbf{x}} \in \check{K}} |\partial_s z_h - \widehat{\partial_s z_h}| \lesssim p^d u \kappa(\partial_s \Phi) \kappa(\partial_s V_{\check{K}}) \|z\|_\infty. \quad (41)$$

Proof. See Appendix A. □

4.2 Geometry evaluation

In this subsection we analyze the propagation of rounding errors in geometry evaluations. We first recall the expressions of the mass and Poisson geometry tensors:

$$\begin{aligned} G(\tilde{\mathbf{x}}) &= |\det(J)|, & (\text{mass form}), \\ G_{ij}(\tilde{\mathbf{x}}) &= |\det(J)| \sum_{k=1}^d (J_{ik}^{-1} J_{jk}^{-1}), & (\text{Poisson form}), \end{aligned} \quad (42)$$

where $J = J(\tilde{\mathbf{x}}) \in \mathbb{R}^{d \times d}$ is the Jacobian matrix. Note that on simplices J and G are constant in space.

Our rounding error analysis proceeds by considering, in turn: 1) Evaluations of the Jacobian (Section 4.2.1). 2) Evaluation of the Jacobian determinant, i.e., the mass form geometry tensor (Section 4.2.2). 3) Evaluation of the Jacobian inverse (Section 4.2.3). 4) Evaluation of the Poisson geometry tensor (Section 4.2.4).

4.2.1 Jacobian evaluations.

We focus on first-order meshes only for simplicity and we analyse the following evaluation algorithm: Let $K \in \mathcal{D}_h$, let $\{\psi_k(\mathbf{x})\}_{k=1}^{n_\psi}$ be the degree-1 Lagrange basis, and let $\{\phi_k(\tilde{\mathbf{x}})\}_{k=1}^{n_\psi}$ be the corresponding reference basis over \hat{K} , the reference cell. Every point in K then satisfies

$$\mathbf{x} = \sum_{k=1}^{n_\psi} \mathbf{x}^k \psi_k(\mathbf{x}) = \sum_{k=1}^{n_\psi} \mathbf{x}^k \phi_k(\tilde{\mathbf{x}}), \quad (43)$$

where \mathbf{x}^k is the k -th vertex of K and $\tilde{\mathbf{x}} \in \hat{K}$. We can use the above to derive an expression for the Jacobian:

$$J_{ij}(\tilde{\mathbf{x}}) = \frac{\partial x_i}{\partial X_j} = \sum_{k=1}^{n_\psi} x_i^k (\partial_j \phi_k(\tilde{\mathbf{x}})). \quad (44)$$

For which the following result holds:

Lemma 4.2. *Let K be a non-degenerate cell with vertices $\{\mathbf{x}^k\}_{k=1}^{n_\psi}$ and let $\mathcal{X} \in \mathbb{R}^{d \times n_\psi}$ with $\mathcal{X}_{ik} = x_i^k$. Let $\{\psi_k(\mathbf{x})\}_{k=1}^{n_\psi}$ be the degree-1 Lagrange basis, and let $\{\phi_k(\tilde{\mathbf{x}})\}_{k=1}^{n_\psi}$ be the corresponding reference basis over the reference cell. Let $J(\tilde{\mathbf{x}})$ be defined as in (44). If u is sufficiently small, the evaluation of J yields instead \hat{J} satisfying, for all $\tilde{\mathbf{x}} \in \hat{K}$,*

$$\hat{J} = J + \Delta J, \quad \text{where} \quad |\Delta J| \leq c_1(d)u \|\mathcal{X}\|_\infty, \quad \|\Delta J\|_\infty \leq c_2(d)u\kappa(K)\|J\|_\infty, \quad \kappa(K) = n_\psi \frac{\|\mathcal{X}\|_\infty}{\|J\|_\infty} \geq 1. \quad (45)$$

Here $c_1(d) > 1$ and $c_2(d) > 1$ are constants that grow exponentially with d .

Proof. The derivatives of degree-1 Lagrange basis functions have simple expressions: on simplices they are constant, while for boxed cells they are products of d monomials and thus satisfy the assumptions of Lemma A.4. Invoking Lemma A.4 we thus obtain the bound

$$\hat{J} = J + \Delta J, \quad \text{where} \quad |\Delta J| \leq \gamma_{n_\psi+d(r+2)} C(\nabla \Phi) \|\mathcal{X}\|_\infty, \quad \text{where} \quad C(\nabla \Phi) = \max_{j, \tilde{\mathbf{x}}} \sum_{k=1}^{n_\psi} |\partial_j \phi_k(\tilde{\mathbf{x}})|. \quad (46)$$

We note that for all types of cells, we have $r = O(1)$. Additionally, it holds that $C(\nabla \Phi) \leq n_\psi \leq 2^d$ since each derivative is bounded in absolute value by 1 for all points on the reference cell. We can thus bound

$$\gamma_{n_\psi+d(r+2)} C(\nabla \Phi) \leq \gamma_{n_\psi^2+d(r+2)} \leq c(d)u, \quad (47)$$

for some constant $c(d) > 1$ which grows exponentially with d . Combining (46) with (47) yields the first bound in (45). To obtain the second bound it is sufficient to take the infinity norm on both sides of the first bound and multiply and divide by $\|J\|_\infty$ (since the cell is non-degenerate by assumption the norm of J is nonzero). The factor n_ψ in the definition of $\kappa(K)$ is there to ensure that $\kappa(K) \geq 1$. Indeed we have $\|J\|_\infty \leq C(\nabla \Phi) \|\mathcal{X}\|_\infty \leq n_\psi \|\mathcal{X}\|_\infty$. \square

Remark 4.2. The bound (45) can be generalized to higher-order meshes by using the analysis from Appendix A to account for derivatives with a higher polynomial degree, but we refrain from doing so here for the sake of simplicity.

Proof. Throughout the proof we ignore d -dependent constants for simplicity and simply write $a \lesssim b$ to indicate that there exists $c(d) \geq 1$ such that $a \leq c(d)b$. By the triangle inequality

$$|\widehat{J^{-1}} - J^{-1}| \leq |\widehat{J^{-1}} - A^{-1}| + |A^{-1} - J^{-1}|. \quad (57)$$

Setting $A = \widehat{J} = J + \Delta J$ and replacing Y with $\widehat{J^{-1}}$ in (6) we can bound the first term on the right and obtain

$$|\widehat{J^{-1}} - J^{-1}| \lesssim u|A^{-1}||A||A^{-1}| + |A^{-1} - J^{-1}|. \quad (58)$$

To leading order in u we have that

$$A^{-1} = (J + \Delta J)^{-1} = A^{-1} - A^{-1}\Delta J A^{-1} + O(u^2), \quad (59)$$

and therefore,

$$|A^{-1}||A||A^{-1}| = |J^{-1}||J||J^{-1}| + O(u), \quad \text{and} \quad |A^{-1} - J^{-1}| = |J^{-1}||\Delta J||J^{-1}| + O(u^2). \quad (60)$$

Replacing the above into (58), ignoring $O(u^2)$ terms and invoking Lemma 4.2 we obtain

$$|\widehat{J^{-1}} - J^{-1}| \lesssim u|J^{-1}||J||J^{-1}| + |J^{-1}||\Delta J||J^{-1}| \lesssim \kappa_2(J)\kappa(K)u|J^{-1}|, \quad (61)$$

which is the thesis. Note that we have used the fact that $|J||J^{-1}| \leq \| |J||J^{-1}| \|_{\max} \leq \|J\|_2 \|J^{-1}\|_2 = \kappa_2(J)$. \square

4.2.4 Poisson geometry.

We can now combine the above bounds to obtain a rounding error estimate for the Poisson geometry tensor.

Theorem 4.5. *Let the assumptions of Theorem 4.3 and Lemma 4.4 hold and let $G \in \mathbb{R}^{d \times d}$ be the Poisson geometry tensor. Its evaluation in precision u yields \widehat{G} satisfying*

$$\widehat{G} = G + \Delta G, \quad \text{where} \quad |\Delta G| \leq c_1(d)u\kappa(K)\kappa_2(J)\widehat{G}(\tilde{\mathbf{x}}), \quad (62)$$

$$\text{and} \quad \|\Delta G\|_{\max} \leq c_2(d)u\kappa(K)\kappa_2(J)\|G\|_{\max}, \quad (63)$$

where $\widehat{G}(\tilde{\mathbf{x}}) = |\det(J)(\tilde{\mathbf{x}})||J^{-1}(\tilde{\mathbf{x}})||J^{-T}(\tilde{\mathbf{x}})|$ and $c_1(d), c_2(d) \geq 1$ are constants growing with d .

Proof. Again, we ignore d -dependent constants in the proof and simply write $a \lesssim b$ to indicate that there exists $c(d) \geq 1$ such that $a \leq c(d)b$. Before we proceed, we write G as

$$G_{ij}(\tilde{\mathbf{x}}) = |\det(J)| \sum_{k=1}^d (J_{ik}^{-1} J_{jk}^{-1}) = |\det(J)| (\mathbf{a}_i^T \mathbf{a}_j), \quad (64)$$

where we have indicated with \mathbf{a}_i^T the i -th row of J^{-1} . Computing G_{ij} in finite precision then yields

$$\widehat{G}_{ij} = |\widehat{\det(J)}| (\widehat{\mathbf{a}}_i^T \widehat{\mathbf{a}}_j) (1 + \delta). \quad (65)$$

In what follows we ignore the $(1 + \delta)$ term for simplicity it does not affect the final bound. To begin with, we require an error bound on the evaluation of \mathbf{a}_i^T , the rows of J^{-1} . Applying Lemma 4.4 yields

$$\widehat{\mathbf{a}}_i = \mathbf{a}_i + \Delta \mathbf{a}_i, \quad \text{where} \quad |\Delta \mathbf{a}_i| \leq c(d)\kappa_2(J)\kappa(K)u|\mathbf{a}_i|. \quad (66)$$

Invoking the inner product bound (3) and Theorem 4.3 gives

$$\widehat{G}_{ij} = |\widehat{\det(J)}| (\widehat{\mathbf{a}}_i^T \widehat{\mathbf{a}}_j) = (|\det(J)| + \Delta_{\text{absdet}}) ((\widehat{\mathbf{a}}_i + \Delta \widehat{\mathbf{a}}_i)^T (\widehat{\mathbf{a}}_j)), \quad (67)$$

where

$$|\Delta \widehat{\mathbf{a}}| \lesssim u|\widehat{\mathbf{a}}_i| \lesssim u(1 + u\kappa_2(J)\kappa(K))|\mathbf{a}_i|, \quad (68)$$

$$|\Delta_{\text{absdet}}| \lesssim \kappa_2(J)\kappa(K)u|\det(J)|. \quad (69)$$

Pulling together all bounds for all perturbation terms we obtain that, to leading order in u ,

$$|\Delta G_{ij}| = |\hat{G}_{ij} - G_{ij}| \lesssim |\det(J)| (|\mathbf{a}_i|^T |\Delta \mathbf{a}_j| + |\Delta \mathbf{a}_i|^T |\mathbf{a}_j| + |\Delta \hat{\mathbf{a}}_i|^T |\mathbf{a}_j|) + |\Delta_{\text{absdet}}| |\mathbf{a}_i|^T |\mathbf{a}_j| \quad (70)$$

$$\lesssim (1 + \kappa_2(J)\kappa(K))u|\det(J)||\mathbf{a}_i|^T |\mathbf{a}_j| \lesssim \kappa_2(J)\kappa(K)u|\det(J)||\mathbf{a}_i|^T |\mathbf{a}_j|. \quad (71)$$

The above yields (62) since $|\mathbf{a}_i|^T |\mathbf{a}_j| = (|J^{-1}| |J^{-T}|)_{ij}$. Furthermore, the same result holds if we replace the absolute value with the 2-norm, which gives

$$\|\Delta G\|_2 \lesssim \kappa_2(J)\kappa(K)u|\det(J)| \| |J^{-1}| |J^{-T}| \|_2. \quad (72)$$

To conclude the proof, we note that

$$|\det(J)|^{-1} \|\tilde{G}\|_2 = \| |J^{-1}| |J^{-T}| \|_2 \leq (\| |J^{-1}| |J^{-T}| \|_1 \| |J^{-1}| |J^{-T}| \|_\infty)^{1/2} \leq \|J^{-1}\|_1 \|J^{-1}\|_\infty \quad (73)$$

$$\leq d \|J^{-1}\|_2^2 = d \|J^{-1} J^{-T}\|_2 = d \|G\|_2 |\det(J)|^{-1}. \quad (74)$$

Plugging the above into (72) yields

$$\|\Delta G\|_{\max} \leq \|\Delta G\|_2 \lesssim u\kappa(K)\kappa_2(J)\|G\|_2 \lesssim u\kappa(K)\kappa_2(J)\|G\|_{\max}, \quad (75)$$

which is (63) and the thesis. \square

Remark 4.3. The analysis developed here should easily generalize to different forms and elements since geometry tensors often include products of entries of J and/or J^{-1} as well as powers of $|\det(J)|$ (see e.g., [39, 54]).

4.3 Mixed-precision construction of local matrices and vectors

We now focus on the evaluation of the matrices and vectors appearing in Algorithms 1 and 2. Here, we consider a mixed-precision implementation in which different precisions are used for different computations. In particular, we employ the precisions in the following list.

List 1. Precisions used in the analysis:

- Precision u_p to tabulate and evaluate basis functions and functions in FE approximation subspaces.
- Precision u_g to compute the geometry tensor (including the polynomial evaluations used to compute J).
- Precision u_q to perform and accumulate the matrix-matrix and matrix-vector products into A and \mathbf{v} respectively.
- Precision u_s with $\max(u_p, u_g, u_q) \leq u_s$ to store B , \mathbf{r}_s , and C , and to compute H .

Including a storage precision u_s is useful as it describes reduced-precision storage strategies and the possible decoupling of memory and computation floating-point formats. Indeed, reducing the storage precision may lead to memory savings as well as better cache use. Furthermore, AMX and tensor core accelerators do perform mixed-precision computations in which the arrays are stored at a lower precision than the arithmetic precision.

We remark that the use of multiple precisions is only a tool for deriving a finer-grained analysis and that we do not necessarily advocate using four different floating-point formats. For instance, it is sufficient to set $u_p = u_g = u_q = u_s$ to obtain a single (in the sense of one) working precision result. In Section 4.5, we will show how these precision can be chosen to tailor our analysis to AMX- and tensor-core-accelerated kernels.

Construction of C . We first focus on the construction of the fourth-order tensor $C \in \mathbb{R}^{n_d \times n_d \times n_q \times n_q}$, which we recall is given by

$$C_{st} = \text{diag}_{q=1}^{n_q} (\omega_q G_{st}(\check{\mathbf{x}}_q) \check{\mathbf{z}}(\check{\mathbf{x}}_q)) \in \mathbb{R}^{n_q \times n_q}, \quad (76)$$

where $s, t \in \{1, \dots, n_d\}$. A forward error bound is given by the following theorem:

Theorem 4.6. *Let the assumptions of Lemma 4.1 hold for the Lagrange basis and let the assumptions of Theorems 4.3 and 4.5 hold for the mass and Poisson form respectively. Let \tilde{G} be as in Theorem 4.5 for Poisson and $\tilde{G} \equiv G$ for the mass form. Let $G(\tilde{\mathbf{x}})$ be evaluated in precision u_g , $\tilde{z}(\tilde{\mathbf{x}}) = \mathbf{z}^T \tilde{\Phi}(\tilde{\mathbf{x}})$ be evaluated with precision u_p and then cast to precision u_g , and C be computed using precision u_g and then rounded to precision u_s . Then, if $\max(u_g, u_p) \leq u_s$, the evaluation of C yields instead \hat{C} satisfying*

$$\hat{C} = C + \Delta C, \quad \text{where} \quad |\Delta C| \lesssim u_s |C| + u_p \Theta^C + c(d) u_g \Gamma^C + O(u_s^2 + (u_g + u_p)^2), \quad (77)$$

Where Θ^C, Γ^C are fourth order tensors of the same sizes and sparsity pattern of C . They are given by

$$\Theta_{st}^C = p^d \kappa(V_{\tilde{K}}) \|\mathbf{z}\|_\infty \text{diag}_{q=1}^{n_q} (|\omega_q G_{st}(\tilde{\mathbf{x}}_q)|), \quad \Gamma_{st}^C = \kappa(K) \text{diag}_{q=1}^{n_q} \left(\kappa_2(J(\tilde{\mathbf{x}}_q)) |\omega_q \tilde{G}_{st}(\tilde{\mathbf{x}}_q) \tilde{z}(\tilde{\mathbf{x}}_q)| \right). \quad (78)$$

If $\tilde{z}(\tilde{\mathbf{x}})$ is constant, the bound holds with $\Theta^C = 0$.

Proof. The evaluation in finite precision of C_{stqq} yields

$$\omega_q (G_{st}(\tilde{\mathbf{x}}_q) + \Delta G_{st}(\tilde{\mathbf{x}}_q)) (\tilde{z}(\tilde{\mathbf{x}}_q) + \Delta \tilde{z}(\tilde{\mathbf{x}}_q)) (1 + \theta_4^q) (1 + \delta^s), \quad (79)$$

where $|\theta_4^q| \leq c u_g$ for some constant $c \geq 4$ and $|\delta^s| < u_s$, $\Delta G_{st} = \hat{G}_{st} - G_{st}$, and $\Delta \tilde{z}(\tilde{\mathbf{x}}_q) = \hat{\tilde{z}}(\tilde{\mathbf{x}}_q) - \tilde{z}(\tilde{\mathbf{x}}_q)$. Here θ_4^q represents the error due to casting $\tilde{z}(\tilde{\mathbf{x}}_q)$ and ω_q to precision u_g as well as the error in the multiplications forming C . The quantity δ^s accounts for the final rounding of C to precision u_s . The evaluation error is thus given by

$$|\hat{C}_{stq} - C_{stq}| \leq |C| (|\theta_4^q| + |\delta_s|) + \bar{c} |\Delta \tilde{z}(\tilde{\mathbf{x}}_q)| |\omega_q G_{st}(\tilde{\mathbf{x}}_q)| + \bar{c} |\omega_q \tilde{z}(\tilde{\mathbf{x}}_q)| |\Delta G_{st}| + O(u_s^2 + (u_g + u_p)^2), \quad (80)$$

where $\bar{c} \geq 1$ is a constant such that we can upper bound $|(1 + \theta_4^q)(1 + \delta_s)| \leq \bar{c}$. We now have that $|\theta_4^q| + |\delta_s| \leq \tilde{c} u_s$ for some $\tilde{c} \geq 1$ since $u_g \leq u_s$ and we can now invoke our previous results to bound all the other quantities appearing in the bounds. Indeed, the quantity $|\Delta G_{st}|$ is bounded as described by Theorem 4.5 (for Poisson) and by Lemma 4.3 (for the mass form since $G_{st} = |\det(J)|$ in this case), while $|\Delta \tilde{z}(\tilde{\mathbf{x}}_q)|$ satisfies the same bound as in equation (40). Therefore, it holds that

$$|\Delta \tilde{z}(\tilde{\mathbf{x}}_q)| \leq \bar{c}_1 p^d u_p \kappa(V_{\tilde{K}}) \|\mathbf{z}\|_\infty, \quad |\Delta G_{st}| \leq \bar{c}_2(d) u_g \kappa(K) \kappa_2(J(\tilde{\mathbf{x}}_q)) |\tilde{G}_{st}(\tilde{\mathbf{x}}_q)|, \quad (81)$$

for some generic constants $\bar{c}_1, \bar{c}_2(d) \geq 1$. Plugging the above into (80) yields the thesis. Note that if $\tilde{z}(\tilde{\mathbf{x}})$ is constant, then $\Delta \tilde{z}(\tilde{\mathbf{x}}) = (1 + \delta_p) \tilde{z}(\tilde{\mathbf{x}})$ for all X where $|\delta_p| \leq u_p \leq u_s$ so we can absorb the error in the evaluation of \tilde{z} into the $O(u_s)$ term in (80) and set $\Theta^C = 0$. \square

Construction of \mathbf{r}_s . A similar result holds for actions, but first let us recall the expression for \mathbf{r}_s :

$$\mathbf{r}_s = \text{vstack}_{q=1}^{n_q} (\omega_q \tilde{z}(\tilde{\mathbf{x}}_q) G(\tilde{\mathbf{x}}_q) \tilde{w}(\tilde{\mathbf{x}}_q)), \quad (\text{mass form}), \quad (82)$$

$$\mathbf{r}_s = \text{vstack}_{q=1}^{n_q} (\omega_q \tilde{z}(\tilde{\mathbf{x}}_q) (G(\tilde{\mathbf{x}}_q) \nabla \tilde{w}(\tilde{\mathbf{x}}_q))), \quad (\text{Poisson form}), \quad (83)$$

where $s = 1, \dots, n_d$. For easiness of notation, we set

$$R = [\mathbf{r}_1 | \dots | \mathbf{r}_{n_d}]. \quad (84)$$

An error bound for the mixed-precision computation of \mathbf{r}_s is given by the following theorem:

Theorem 4.7. *Let the assumptions of Lemma 4.1 hold for the Lagrange basis and let the assumptions of Theorems 4.3 and 4.5 hold for the mass and Poisson form respectively. Let \tilde{G} be as in Theorem 4.5. Let $G(\tilde{\mathbf{x}})$ be evaluated in precision u_g , $\tilde{z}(\tilde{\mathbf{x}}) = \mathbf{z}^T \tilde{\Phi}(\tilde{\mathbf{x}})$, $\tilde{w}(\tilde{\mathbf{x}}) = \mathbf{w}^T \tilde{\Phi}(\tilde{\mathbf{x}})$ and $\nabla \tilde{w}(\tilde{\mathbf{x}})$ be evaluated with precision u_p and then cast to precision u_g , and \mathbf{r}_s be computed using precision u_g and then rounded to precision u_s . Then, if $\max(u_g, u_p) \leq u_s$, the evaluation of R yields instead \hat{R} satisfying*

$$\hat{R} = R + \Delta R, \quad \text{where} \quad |\Delta R| \lesssim u_s |R| + u_p \Theta^R + c(d) u_g \Gamma^R + O(u_s^2 + (u_g + u_p)^2). \quad (85)$$

If $\tilde{z}(\tilde{\mathbf{x}})$ is constant, then the same bound holds after replacing $\|\mathbf{z}\|_\infty$ with zero. Here $\Theta^R, \Gamma^R \in \mathbb{R}^{n_q \times n_d}$. For the mass form, these are given entrywise by

$$\Theta_{qs}^R = p^d \kappa(V_{\tilde{K}}) (|\tilde{w}(\tilde{\mathbf{x}}_q)| \|\mathbf{z}\|_\infty + |\tilde{z}(\tilde{\mathbf{x}}_q)| \|\mathbf{w}\|_\infty) |\omega_q G(\tilde{\mathbf{x}}_q)|, \quad \Gamma_{qs}^R = \kappa(K) \kappa_2(J(\tilde{\mathbf{x}}_q)) |R_{sq}|, \quad (86)$$

while for the Poisson form it holds

$$\Theta_{qs}^R = p^d |\omega_q| \left(\kappa(V_{\tilde{K}}) \|\mathbf{z}\|_\infty (|G(\tilde{\mathbf{x}}_q) \nabla \tilde{w}(\tilde{\mathbf{x}}_q)|) + |\tilde{z}(\tilde{\mathbf{x}}_q)| \|\mathbf{w}\|_\infty \left(|G(\tilde{\mathbf{x}}_q)| [\kappa(\partial_k \tilde{\Phi}) \kappa(\partial_k V_{\tilde{K}})]_{k=1}^d \right) \right)_s, \quad (87)$$

$$\Gamma_{qs}^R = \kappa(K) \kappa_2(J(\tilde{\mathbf{x}}_q)) |\omega_q \tilde{z}(\tilde{\mathbf{x}}_q)| (|\tilde{G}(\tilde{\mathbf{x}}_q)| |\nabla \tilde{w}(\tilde{\mathbf{x}}_q)|)_s. \quad (88)$$

Proof. The proof for the mass form is essentially the same as the one of Theorem 4.6 and we thus omit it. The only difference is the extra $\tilde{w}(\tilde{\mathbf{x}}_q)$ term which leads to the $(\|\tilde{w}(\tilde{\mathbf{x}}_q)\|_{\mathbf{z}}\|_{\infty} + \|\tilde{z}(\tilde{\mathbf{x}}_q)\|_{\mathbf{w}}\|_{\infty})$ term in the bound for Θ^R .

We now consider the Poisson form. We start by analyzing the errors arising from $G\nabla\tilde{w}$. Owing to the error bound for matrix-vector products (cf. (4)) it holds that

$$(\widehat{G\nabla\tilde{w}})_s = ((\hat{G} + \Delta\hat{G})\widehat{\nabla\tilde{w}})_s = \left((G + \Delta G + \Delta\hat{G})(\nabla\tilde{w} + (\widehat{\nabla\tilde{w}} - \nabla\tilde{w})) \right)_s (1 + \delta_g), \quad (89)$$

where $(1 + \delta_g)$ accounts for the rounding of $\nabla\tilde{w}$ to precision u_g and the term $|\widehat{\nabla\tilde{w}} - \nabla\tilde{w}|$ accounts for the error of evaluating $\nabla\tilde{w}$ at precision u_p , which can be bound using equation (41) of Lemma 4.1. Here the quantity ΔG satisfies the bound of Theorem 4.5, $|\Delta\hat{G}| \lesssim u_g|G|$ due to equation (4), and $|\delta_g| < u_g$. Pulling all these results together, we obtain

$$\begin{aligned} |\widehat{G\nabla\tilde{w}} - G\nabla\tilde{w}| &\leq |G||\widehat{\nabla\tilde{w}} - \nabla\tilde{w}| + |\Delta G||\nabla\tilde{w}| + c(d)u_g|G\nabla\tilde{w}| + O((u_g + u_p)^2) \\ &\lesssim p^d u_p |G| [\kappa(\partial_k \Phi) \kappa(\partial_k V_{\tilde{K}})]_{k=1}^d \|\mathbf{w}\|_{\infty} + c(d)u_g \kappa(K) \kappa_2(J) |\tilde{G}||\nabla\tilde{w}| + O((u_g + u_p)^2), \end{aligned} \quad (90)$$

where $c(d) \geq 1$ and we have omitted the $\tilde{\mathbf{x}}_q$ -dependency for easiness of notation. In the above, the first term on the right-hand side bounds $|G||\widehat{\nabla\tilde{w}} - \nabla\tilde{w}|$ and is a consequence of taking the infinity norm of (41). The second term instead bounds $|\Delta G||\nabla\tilde{w}|$ and is a consequence of Theorem 4.5. In (90) the term $c(d)u_g|G||\nabla\tilde{w}|$ was absorbed into $c(d)$ since $|G| \leq |\tilde{G}|$ by Theorem 4.5.

Turning to the evaluation of R , we have that

$$\hat{R}_{qs} = \omega_q(\tilde{z}(\tilde{\mathbf{x}}_q) + \Delta\tilde{z}(\tilde{\mathbf{x}}_q))(G\nabla\tilde{w} + (\widehat{G\nabla\tilde{w}} - G\nabla\tilde{w}))(1 + \theta_4^g)(1 + \delta_s), \quad (91)$$

where $\Delta\tilde{z}(\tilde{\mathbf{x}}_q)$ is the error in the evaluation of $\tilde{z}(\tilde{\mathbf{x}}_q)$ at precision u_p and can be bound using Lemma 4.1. Note that the expression above is in the same form as equation (80) and it can thus be bound using the same procedure and by applying (90). The result reads

$$\begin{aligned} |\hat{R}_{qs} - R_{qs}| &\lesssim u_s |R_{qs}| \\ &+ p^d u_p |\omega_q| \left(\|\tilde{z}(\tilde{\mathbf{x}}_q)\|_{\mathbf{w}}\|_{\infty} |G(\tilde{\mathbf{x}}_q)| [\kappa(\partial_k \Phi) \kappa(\partial_k V_{\tilde{K}})]_{k=1}^d + \kappa(V_{\tilde{K}})\|\mathbf{z}\|_{\infty} |G(\tilde{\mathbf{x}}_q)\nabla\tilde{w}(\tilde{\mathbf{x}}_q)| \right) \\ &+ c(d)u_g \kappa(K) \kappa_2(J(\tilde{\mathbf{x}}_q)) |\omega_q \tilde{z}(\tilde{\mathbf{x}}_q)| (|\tilde{G}(\tilde{\mathbf{x}}_q)||\nabla\tilde{w}(\tilde{\mathbf{x}}_q)|)_s + O(u_s^2 + (u_g + u_p)^2), \end{aligned} \quad (92)$$

which is the thesis. \square

Remark 4.4. In Theorems 4.6 and 4.7 we have assumed that all functions belong to the same finite element approximation space for simplicity. The same results as in Theorems 4.6 and 4.7 hold, albeit with slightly different values for Θ^C and Θ^R , if different FE approximation spaces are used in the same form.

Construction of B and H . The entries of B are simply the values of the basis functions (for the mass form) or their derivatives (for Poisson) at the quadrature nodes. Thus, Lemma 4.1 directly applies⁸ and the evaluation of B at precision $u_p \leq u_s$ yields instead \tilde{B} which satisfies, ignoring constants,

$$|\tilde{B} - B| \lesssim dp u_p |B| = u_p \Theta^B, \quad (\text{mass form}), \quad (93)$$

$$|\tilde{B}_{skq} - B_{skq}| \lesssim dp u_p \kappa(\partial_s \phi_k) \max_i |B_{ski}| = u_p \Theta_{skq}^B, \quad (\text{Poisson form}), \quad (94)$$

where Θ^B is a third-order tensor of the same shape as B . Rounding the result to precision u_s yields \hat{B} satisfying

$$\hat{B} = B + \Delta B, \quad \text{with} \quad |\Delta B| \lesssim u_s |B| + u_p \Theta^B + O(u_s^2). \quad (95)$$

As far as $H_{st} = C_{st} B_t^T$ is concerned, its entries are given by

$$H_{stqk} = C_{stq} B_{tkq}, \quad (96)$$

where $s, l \in \{1, \dots, n_d\}$. Thus, invoking Theorem 4.6, we obtain for the computation of H_{stqk} at precision u_s ,

$$\hat{H} = H + \Delta H, \quad \text{where} \quad |\Delta H| \lesssim u_s |H| + u_p \Theta^H + c(d)u_g \Gamma^H + O(u_s^2 + (u_g + u_p)^2), \quad (97)$$

where $\Theta_{stqk}^H = \Theta_{stq}^C + \Theta_{tkq}^B$ and $\Gamma_{stqk}^H = \Gamma_{stq}^C$ for all $s, t \in \{1, \dots, n_d\}$, $k = 1, \dots, n_\phi$, $q = 1, \dots, n_q$.

⁸For Poisson, we take the max of $|\partial_s \phi_k(\tilde{\mathbf{x}})|$ with respect to the quadrature nodes rather than over the whole reference cell. This is a minimal variation of the result in Lemma 4.1 and does not affect its proof.

4.4 Mixed-precision accumulation of products into A and v and global assembly

4.4.1 Full local kernel error bounds

We are now ready for the last step in our error analysis: the accumulation of matrix and vector products into the local matrix and vector A and v . We present both results at the same time since their proofs are similar:

Theorem 4.8. *Let the assumptions of Theorem 4.6 hold and assume that the matrix-matrix products and their accumulation into A are performed at precision $u_q \leq u_s$. Then, the mixed-precision computation of A using the precisions described in List 1 yields instead \hat{A} satisfying*

$$|\hat{A} - A| \lesssim (u_s + (n_d^2 + n_q)u_q) \sum_{s=1}^{n_d} \sum_{t=1}^{n_d} |B_s| |H_{st}| + u_p \Theta^A + c(d)u_g \Gamma^A + O(u_s^2 + (u_q + u_g + u_p)^2), \quad (98)$$

where $\Theta^A, \Gamma^A \in \mathbb{R}^{n_\phi \times n_\phi}$ are given by

$$\Theta^A = \sum_{s=1}^{n_d} \sum_{t=1}^{n_d} (|B_s| \Theta_{st}^H + \Theta_s^B |H_{st}|), \quad \Gamma^A = \sum_{s=1}^{n_d} \sum_{t=1}^{n_d} |B_s| \Gamma_{st}^H. \quad (99)$$

Theorem 4.9. *Let the assumptions of Theorem 4.7 hold and assume that the matrix-vector products and their accumulation into v are performed at precision $u_q \leq u_s$. Then, the mixed-precision computation of v using the precisions described in List 1 yields instead \hat{v} satisfying*

$$|\hat{v} - v| \lesssim (u_s + (n_d + n_q)u_q) \sum_{s=1}^{n_d} |B_s| |\mathbf{r}_s| + u_p \Theta^v + c(d)u_g \Gamma^v + O(u_s^2 + (u_q + u_g + u_p)^2), \quad (100)$$

where $\Theta^v, \Gamma^v \in \mathbb{R}^{n_\phi}$ are vectors given by

$$\Theta^v = \sum_{s=1}^{n_d} (|B_s| \Theta_s^R + \Theta_s^B |\mathbf{r}_s|), \quad \Gamma^v = \sum_{s=1}^{n_d} |B_s| \Gamma_s^R. \quad (101)$$

Here Θ_s^R and Γ_s^R denote the s -th column of Θ^R and Γ^R respectively.

Proof. The proof of both theorems is essentially the same since the forward bound for matrix-matrix products in (5) also holds for matrix-vector products. Therefore, we only prove Theorem 4.8. We have that

$$\hat{A} = \sum_{s=1}^{n_d} \sum_{t=1}^{n_d} ((B_s + \Delta B_s)(H_{st} + \Delta H_{st}) + \Delta A_{st}) \left(1 + \theta_{n_d^2}^q\right), \quad (102)$$

where $|\Delta B_s|$ satisfies (95) and $|\Delta H_{st}|$ satisfies (97). Here, $\theta_{n_d^2}^q$ is the error due to the summations, bounded according to $|\theta_{n_d^2}^q| \lesssim n_d^2 u_q$, and ΔA_{st} is the error from the matrix-matrix product which satisfies the bound (cf. equation (5))

$$|\Delta A_{st}| \lesssim n_q u_q |B_s + \Delta B_s| |H_{st} + \Delta H_{st}| = n_q u_q |B_s| |H_{st}| + O(u_q(u_s + u_p + u_g)). \quad (103)$$

Therefore

$$|\hat{A} - A| \lesssim \sum_{s=1}^{n_d} \sum_{t=1}^{n_d} (|B_s| |\Delta H_{st}| + |\Delta B_s| |H_{st}| + (n_d^2 u_q + n_q u_q) |B_s| |H_{st}|) + O(u_s^2 + (u_q + u_g + u_p)^2). \quad (104)$$

Replacing $|\Delta B_s|$ and $|\Delta H_{st}|$ with their respective upper bounds (cf. (95) and (97)) yields the thesis. To prove Theorem 4.9, the same proof follows with the following modifications: Replace n_d^2 with n_d (since there are only n_d terms in the sum), H_{st} with \mathbf{r}_s , and invoke Theorem 4.7 in replacement of equation (97). \square

Since it may be difficult to keep track of all error terms appearing in Theorems 4.8 and 4.9, for the sake of clarity we condense and simplify the main results in Corollary 4.10. We first define the following condition numbers:

$$\kappa_q^A = \frac{\|\sum_{s=1}^{n_d} \sum_{t=1}^{n_d} |B_s| |H_{st}|\|_{\max}}{\|A\|_{\max}}, \quad \kappa_q^v = \frac{\|\sum_{s=1}^{n_d} |B_s| |\mathbf{r}_s|\|_{\infty}}{\|v\|_{\infty}}, \quad (105)$$

$$\kappa_p^A = \frac{\|\Theta^A\|_{\max}}{\|A\|_{\max}}, \quad \kappa_p^v = \frac{\|\Theta^v\|_{\infty}}{\|v\|_{\infty}}, \quad \kappa_g^A = \frac{\|\Gamma^A\|_{\max}}{\|A\|_{\max}}, \quad \kappa_g^v = \frac{\|\Gamma^v\|_{\infty}}{\|v\|_{\infty}}, \quad (106)$$

whose meaning is described as follows:

- κ_q^A and κ_q^v , are the condition numbers in the max and infinity norm of the sum and accumulation of the products into A and v respectively.
- κ_p^A and κ_p^v represent the conditioning of the kernels with respect to the evaluation of the finite element (basis) functions and their derivatives.
- κ_g^A and κ_g^v represent the conditioning of the kernels with respect to geometry computations.

We can now state the corollary:

Corollary 4.10. *Let the assumptions of Theorems 4.8 and 4.9 be satisfied. The mass and Poisson kernels evaluated in mixed-precision according to the precisions in List 1 yield the local matrix and vector \hat{A} and \hat{v} satisfying the following error bounds:*

$$\|\hat{A} - A\|_{\max} \lesssim ((u_s + n_q u_q) \kappa_q^A + u_p \kappa_p^A + u_g \kappa_g^A) \|A\|_{\max}, \quad (107)$$

$$\|\hat{v} - v\|_{\infty} \lesssim ((u_s + n_q u_q) \kappa_q^v + u_p \kappa_p^v + u_g \kappa_g^v) \|v\|_{\infty}. \quad (108)$$

Proof. Apply the max and infinity norm to the bounds in Theorems 4.8 and 4.9 and multiply and divide by $\|A\|_{\max}$ and $\|v\|_{\infty}$ respectively. \square

Remark 4.5. Recalling previous results from this section (Theorems 4.6, 4.7, 4.8, and 4.9), we note that the condition numbers κ_g^A and κ_g^v are both proportional to the condition number of the Jacobian of the reference map:

$$\kappa_g^A, \kappa_g^v \propto \max_q \kappa_2(J(\tilde{x}_q)). \quad (109)$$

Thus, ill-conditioned Jacobians, e.g., due to knife elements, may lead to loss of accuracy.

Remark 4.6. Again, backtracking the values of the condition numbers κ_p^A and κ_p^v through Theorems 4.6, 4.7, 4.8, and 4.9, we note that κ_p^A and κ_p^v are proportional to $p^d \kappa(V_{\tilde{K}})$ for both forms. For the Poisson form it also holds that

$$\kappa_p^A \propto p^d \kappa(V_{\tilde{K}}) + dp \max_k \kappa(\partial_k \Phi), \quad (110)$$

$$\kappa_p^v \propto p^d \kappa(V_{\tilde{K}}) + dp \max_k \kappa(\partial_k \Phi) + \max_k (\kappa(\partial_k \Phi) \kappa(\partial_k V_{\tilde{K}})). \quad (111)$$

Poorly conditioned reference basis functions and high-degree polynomials may thus lead to loss of accuracy.

4.4.2 Global assembly error bounds

We now extend the error bounds in Theorems 4.8 and 4.9 to a rounding error bound for global assembly:

Corollary 4.11. *Let the assumptions of Theorems 4.8 and 4.9 be satisfied for all cells in D_h for local cell matrices and vectors respectively. Let D and \mathbf{b} (defined in (36)) be computed in mixed-precision according to the precisions listed in List 1. Let all cell contributions be assembled into global tensors $A^g = LDL^T$, $\mathbf{v}^g = L\mathbf{b}$ at precision u_q . If L , defined in (36), has at most m_K nonzero entries⁹ per row, it holds that*

$$|\hat{A}^g - A^g| \leq L|\hat{D} - D|L^T + 2cm_K u_q L|D|L^T + O(u_q(u_s + u_q + u_g + u_p)), \quad (112)$$

$$|\hat{\mathbf{v}}^g - \mathbf{v}^g| \leq L|\hat{\mathbf{b}} - \mathbf{b}| + cm_K u_q L|\mathbf{b}| + O(u_q(u_s + u_q + u_g + u_p)). \quad (113)$$

Proof. We only prove the result for A^g since the proof for \mathbf{v}^g is essentially the same. To leading order, we can write

$$\hat{A}^g = L(\hat{D} - D)L^T + \widehat{LDL^T}, \quad (114)$$

where the last term on the right-hand side only accounts for the error in the matrix-matrix products and not in the computation of D . We can then invoke equation (5) twice to bound the two matrix-matrix products. Doing so yields

$$\widehat{LDL^T} = LDL^T + \Delta(LDL^T), \quad \text{where} \quad |\Delta(LDL^T)| \leq 2\gamma_{m_K} L|D|L^T + O(u_q^2). \quad (115)$$

⁹Another equivalent definition of m_k : it is the maximum number of local degrees of freedom that correspond to the same global degree of freedom.

The above bound is due to the fact that L is boolean and sparse with at most m_K ones per row and thus: 1) $L = |L|$, 2) L is representable exactly, 3) The action of L from the left and of L^T from the right against D yields a matrix whose entries are the result of a sum of no more than m_K terms. We thus have, to leading order,

$$|\hat{A}^g - A^g| \leq L|\hat{D} - D|L^T + 2cm_K u_q L|D|L^T, \quad (116)$$

which is the thesis. The result for \mathbf{v}^g follows the same exact strategy, but comes without the factor 2 since no multiplication by L^T is performed. \square

The above corollary implies that the error in the global assembly is roughly proportional to the sum of the errors of the local cell tensors. We make this proportionality clearer with an analogous of Corollary 4.10, which shows that the same bound as for the local cell tensors holds, albeit with m_K^2 and m_K times larger factors for bilinear and linear forms respectively:

Corollary 4.12. *Let the assumptions of Corollary 4.11 hold. The global assembly of mass and Poisson kernels evaluated in mixed-precision according to the precisions in List 1 yield the global matrix and vector \hat{A}^g and $\hat{\mathbf{v}}^g$ satisfying:*

$$\|\hat{A}^g - A^g\|_{\max} \lesssim m_K^2 \left((u_s + n_q u_q) \bar{\kappa}_q^A + u_p \bar{\kappa}_p^A + u_g \bar{\kappa}_g^A \right) \|A^g\|_{\max}, \quad (117)$$

$$\|\hat{\mathbf{v}}^g - \mathbf{v}^g\|_{\infty} \lesssim m_K \left((u_s + n_q u_q) \bar{\kappa}_q^v + u_p \bar{\kappa}_p^v + u_g \bar{\kappa}_g^v \right) \|\mathbf{v}^g\|_{\infty}. \quad (118)$$

Here $\bar{\kappa}_t^A \|A^g\|_{\max} = \max_k (\kappa_t^A \|A^k\|_{\max})$ and $\bar{\kappa}_t^v \|\mathbf{v}^g\|_{\infty} = \max_k (\kappa_t^v \|\mathbf{v}^k\|_{\infty})$ for $t \in \{q, p, g\}$.

Proof. We ignore the $O(u_q)$ terms in Corollary 4.11 since they are of negligible size. We thus bound, ignoring higher-order terms,

$$\|\hat{A}^g - A^g\|_{\max} \leq \|L|\hat{D} - D|L^T\|_{\max} \leq m_K^2 \|\hat{D} - D\|_{\max} \quad (119)$$

$$\|\hat{\mathbf{v}}^g - \mathbf{v}^g\|_{\infty} \leq \|L|\hat{\mathbf{b}} - \mathbf{b}\|_{\infty} \leq m_K \|\hat{\mathbf{b}} - \mathbf{b}\|_{\infty}. \quad (120)$$

Since each entry in $L|\hat{D} - D|L^T$ is a sum of at most m_K^2 entries of $|\hat{D} - D|$ and each entry of $L|\hat{\mathbf{b}} - \mathbf{b}|$ is a sum of at most m_K entries of $|\hat{\mathbf{b}} - \mathbf{b}|$. The thesis then readily follows by applying Corollary 4.10 to the above, taking the max across all cells, and multiplying and dividing by $\|A^g\|_{\max}$ and $\|\mathbf{v}^g\|_{\infty}$ respectively. \square

4.5 Mixed-precision strategy and hardware accelerators

We have derived a fine-grained error bound for mixed-precision kernel and assembly computations which allows for different precision choices. In this subsection we make our exposition simpler and more specific by restricting the precision choice to two formats: a low-precision format (e.g., single or half precision) u and a higher-precision format (e.g., single or double) u^2 . The objective here is to choose precisions so as to obtain accurate enough computations while keeping costs contained.

Remark 4.7. From now on, we focus on 3D high-polynomial degree implementations ($p \geq 3$). The reason is that in low dimensions and for low-degree polynomials all kernel computations have roughly the same cost and the different error terms are more or less of comparable size: a mixed-precision implementation of Algorithms 1 and 2 would thus lead to little practical benefits. Furthermore, low-dimension/low-degree kernels are extremely cheap already. We leave the investigation of performant mixed-precision implementations of low-dimension/low-degree kernels to future work.

The first decision we make is the following:

- **Store tensors in reduced precision.** Set $u_s = u$. *Reason:* the error term associated with storage has the smallest constant. Furthermore, reduced-precision storage leads to memory savings and better cache usage.

To guide our next precision choices, we first run the kernels in double precision and time each computational component. Taking the Poisson kernels on hexahedra ($z(\mathbf{x}) \equiv 1$, cell batch size of 16 for actions) as a representative example, we show these results in Figure 1. The cost distribution for the mass kernel and tetrahedra is similar (not shown). For bilinear forms the bottleneck is always the accumulation of matrix-matrix products into A . On the other hand, the evaluation of FE functions accounts for the majority of the total cost of action kernels for low to medium p , while for large p the matrix-matrix product accumulation and the FE function evaluations are both bottlenecks.

A sensible criterion for designing a mixed-precision implementation is to employ the high-precision format for all computations that are either 1) of negligible cost or that 2) lead to the largest rounding errors. These considerations lead to the following decisions:

Poisson on hexahedra, cost distribution

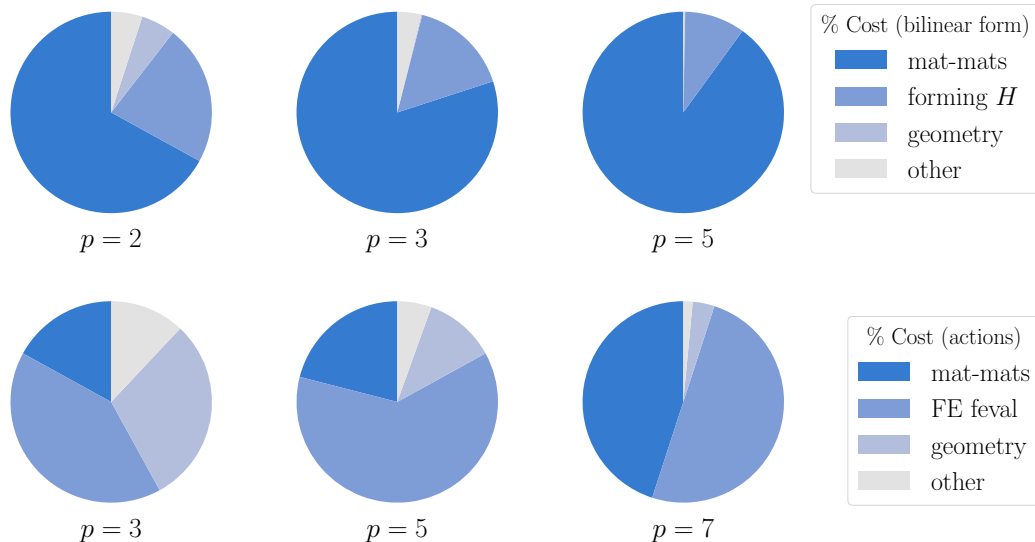


Figure 1: Pie charts of the computational cost distribution of different Poisson kernel subroutines on hexahedra. The results, entirely run in double precision, are shown for different polynomial degrees p . The top and bottom rows correspond to the Poisson bilinear form and action respectively. By “mat-mats” we indicate the cost of accumulating the matrix-matrix products into A and \mathbf{v} and by “FE feval” we denote the evaluation of $\nabla\tilde{u}(\tilde{\mathbf{x}})$.

- **Use high-precision for geometry computations.** Set $u_g = u^2$. *Reason:* Geometry computations are of negligible cost for moderate-to-high degree elements (cf. Figure 1), so a higher-precision implementation does not affect runtime. Furthermore, computing geometry tensors more accurately safeguards kernels from knife elements and ill-conditioned Jacobians.
- **Use high-precision for polynomial evaluations.** Use precision u^2 for tabulation. *Reason:* FE basis functions are tabulated only once and for all in Algorithms 1 and 2 and thus the cost of this operation is typically negligible. Furthermore, the memory access costs of tabulating high-degree polynomials are minimized thanks to the reduced-precision storage.

There are still two precisions to be chosen: The precision of FE function evaluations and the precision used for performing and accumulating the matrix-matrix products into the local tensors A and \mathbf{v} . The issue is that these operations are at the same time the computational bottlenecks of the kernels (cf. Figure 1) and possibly the dominating sources of rounding errors. Indeed, if we recall Corollary 4.10 and Remarks 4.5 and 4.6, these terms lead to rounding errors growing like $p^d u_p$ and $n_q u_q$ respectively and thus rapidly grow with the polynomial degree. Fortunately, there is a way of obtaining high-accuracy computations at a lower cost:

- **Use mixed-precision accelerators for FE function evaluations and matrix-matrix products.** Set $u_p = u^2$ and $u_q = u^2$. *Reason:* Mixed-precision vector and tensor accelerators perform high-precision vector and tensor operations between operands stored at low precisions. The resulting computational cost of these operations is typically lower than the corresponding fully high-precision computations.

Remark 4.8. In some architectures the most performant (if not the only) tensor cores available may be mixed-precision cores [20] and thus the strategy of storing tensors in low precision and multiplying them in high (or mixed) precision may be the only option for exploiting these accelerators.

The above precision selections lead to a mixed-precision kernel implementation with mixed-precision accelerators that satisfies an error bound in the form (cf. Corollary 4.10):

$$\text{relative error} \lesssim u\kappa_q + O(u^2), \quad (121)$$

where κ_q stands for either κ_q^A or κ_q^v . To leading order, the above bound is thus independent from the conditioning of polynomial evaluations and geometry computations. Furthermore, the bound is also independent¹⁰ from the

¹⁰Excluding the condition number κ_q which may or may not hide some p or n_q dependency. In our numerical experiments (cf. Section 5) it seems like it does not, at least for the mass and Poisson forms.

polynomial degree and the number of quadrature nodes. The relative error bound for the assembly is m_K^2 times larger for bilinear forms and m_K times larger for linear forms (actions), cf. 4.12.

Remark 4.9. We remark that using mixed-precision accelerators for FE function evaluations leads to a slight departure from our theory. Indeed, for the sake of simplicity we have not accounted for the error arising from rounding the function coefficients and the tabulated basis function values to a lower precision before performing the evaluation. This casting results in an additional error term in the bounds of Theorems 4.8 and 4.9 which is proportional to the conditioning of the polynomial basis:

$$\propto u_s \kappa(V_{\tilde{K}}), \quad \text{for bilinear forms with coefficients and mass actions,} \quad (122)$$

$$\propto u_s (\kappa(V_{\tilde{K}}) + \max_s \kappa(\partial_s V_{\tilde{K}})), \quad \text{for Poisson actions.} \quad (123)$$

The constants in these error terms are much smaller than in the polynomial evaluation terms in Theorems 4.8 and 4.9 since p^d does not appear as a multiplicative factor. Nevertheless, one must double check that the conditioning of the FE basis does not affect results: while $\kappa(V_{\tilde{K}})$ is typically small provided that the basis is constructed accordingly [36], $\max_s \kappa(\partial_s V_{\tilde{K}})$ could potentially be large, especially on tetrahedra. Nevertheless, we have not found this to be an issue in our numerical experiments (cf. Figure 5, bottom). In any case, the bounds in Corollaries 4.10 and 4.12 and in equation (121) still hold as-is albeit with a larger condition number multiplying the u_s term.

Remark 4.10. The multiplication of large matrices and vectors with tensor and vector accelerators must be blocked, i.e., decomposed into smaller matrix products so that each submatrix and subvector can fit within the accelerator registers. Blocking is beneficial from a rounding error viewpoint as it leads to smaller error constants [10, 11]. Nevertheless, we have ignored blocking effects in our analysis since these only affect the constants of the negligible $O(u^2)$ terms.

5 Numerical results

In this section we validate the rounding error analysis of Section 4 and we test the efficiency and accuracy of hardware accelerated mixed-precision kernel implementations. The aim is to establish the computational superiority of kernels exploiting matrix product accelerators and to compare their accuracy with kernels implemented in different precisions. Specifically, we will show that AMX-accelerated kernels are up to 60 times faster than their double precision equivalents and up to hundreds of times more accurate than fully half-precision kernels.

Here we do not investigate the rounding error behaviour of polynomial and FE function evaluations for the sake of brevity: The evaluation of polynomials is a classical subject in rounding error analysis and its rounding error behaviour has been thoroughly documented (see e.g., Section 5 in [29] and [30, 51]). Similarly, the evaluation of FE functions consists of an inner product (between coefficients and basis functions) whose rounding error analysis is also classical, see e.g., Section 3.1 in [29].

5.1 Experimental setup.

All experiments were performed on a single core of an Intel Xeon Platinum 8480+ processor (code name ‘‘Sapphire Rapids’’) which supports mixed-precision single/bf16 precision vector instructions (AVX512-bf16) as well as matrix multiplication instructions (AMX-bf16). However, we found the overall bf16 intrinsics and compiler support to be limited. Circumventing these limitations warranted specific implementation choices which we describe in Appendix B.

We employed the FEniCSx open-source FE software library [8] (Basix in particular [55, 56]) to tabulate the FE basis functions and to compute the quadrature rules offline and in double precision. All kernels were implemented in C++ in the C++23 standard and compiled using g++ (GCC version 14.2.0) with the compiler flags

```
-std=c++23 -march=sapphirerapids -O3 -mprefer-vector-width=512.
```

All kernels were validated via comparison with the FEniCSx built-in double precision kernels which was also used to compute rounding errors. The open-source code implementing the experiments is freely available on GitHub¹¹. For our numerical computations we exclusively work in three dimensions and employ an unstructured hexahedral mesh of a tetrahedron of coordinates

$$\{(-5, 0, -5), (5, 0, -5), (0, -5, 5), (0, 5, 5)\},$$

¹¹See <https://github.com/croci/mpfem-paper-experiments-2024>.

and an unstructured tetrahedral mesh of the cube $[0, 5]^d$. Both meshes were generated using the open source mesh-generation software Gmsh [26] and have $n_K = 55296$ and $n_K = 63408$ hexahedral and tetrahedral cells respectively. In order to keep the overall computational costs contained even at high-degree polynomial degrees we only run the kernels on the first \tilde{n}_K cells, where \tilde{n}_K is given by the formula

$$\tilde{n}_K = n_{\text{batch}} \lfloor \min(2 \times 10^6 / n_\phi, n_K) / n_{\text{batch}} \rfloor.$$

Here, we recall, n_K is the total number of cells in the mesh, n_ϕ is the number of cell degrees of freedom and n_{batch} is the number of cells batched together in action kernels. The number 2×10^6 is a number large enough to ensure cache spillover to the RAM. This choice prevents the CPU from keeping all data in cache and thus ensures a fair comparison among kernels. The division, floor, and multiplication by n_{batch} is made for convenience to ensure that the number of cells is a multiple of n_{batch} . In our computations we use $n_{\text{batch}} = 64$ which we found gives good performance. With this choice, the above formula yields $\tilde{n}_K = n_K$ only for $p = 2$ for the hexahedral mesh and for $p \in \{2, 3\}$ for the tetrahedral mesh. In our experiments we only consider polynomial degrees larger than 1 and up to degree 10 for tetrahedra and up to degree 7 for hexahedra. These upper bounds were arbitrarily chosen to keep the overall computational time of our single-core experiments contained. As reference cells we take the unit cube $[0, 1]^3$ and the tetrahedron with vertices

$$(0, 0, 0), \quad (1, 0, 0), \quad (0, 1, 0), \quad (0, 0, 1). \quad (124)$$

We set $\tilde{z}(\mathbf{x}) \equiv 1$ for all experiments since the effect of FE function evaluations can already be observed in the action kernels.

5.2 Geometry errors.

We begin by analyzing the rounding error behaviour of geometry computations. Our aim to establish the linear growth of the error with respect to $\kappa_2(J)$ and thus validate the bounds of Theorem 4.5. We only consider the Poisson geometry for the sake of brevity and since results are similar. We start from a tetrahedron of coordinates

$$(1, 1, 0), \quad (1, 0, 1), \quad (\epsilon, 1, -1), \quad (0, 0, 0), \quad (125)$$

where $\epsilon > 0$ is a constant used to tweak the Jacobian condition number. In fact, the resulting Jacobian is

$$\begin{bmatrix} 1 & 1 & 0 \\ 1 & 0 & 1 \\ \epsilon & 1 & -1 \end{bmatrix}, \quad (126)$$

which is singular for $\epsilon = 0$, has $\det(J) = \epsilon$ and $\kappa_\infty(J) = (2 + \epsilon)(3 + \epsilon)/\epsilon$ (and therefore $\kappa_2(J) \propto \frac{1}{\epsilon}$). We then scale the coordinates by $3^{-1/2}$ and translate them by the translation vector $(1/3, 2/3, 4/3)$ so that the transformed cell coordinates and Jacobian stop being exactly representable (this transformation leaves the condition number unchanged). We monitor the relative rounding error in the max norm

$$\frac{\|G - \hat{G}\|_{\max}}{u\|G\|_{\max}}, \quad (127)$$

as a function of the condition number $\kappa_2(J)$, where \hat{G} is computed using exclusively fp32 single precision arithmetic. Results are shown in Figure 2 which match what predicted by the theory. We remark that the powers of ten on the y axis indicate the number of digits lost in the computation. For single precision we have roughly 7.5 digits of accuracy and the proportionality constant seems to be around 0.1 for this cell so geometry computations are safe in this case up to condition numbers of roughly $10^{8.5}$. While we expect similar results to hold for fp16 half precision arithmetic we report that the computation underflows for this precision (results not shown). We nevertheless predict that fp16 would lead to complete loss of accuracy much earlier for condition numbers of only $10^{4.5}$. Mitigation of range issues via scaling is likely possible, but outside the scope of this work (if the CPU supported it here we would have just used bf16 which has a wider range). Nevertheless these results show how using higher precision for geometry computations might be beneficial, especially when the floating-point format has a narrow range or a large unit roundoff.

Remark 5.1. We remark that severely ill-conditioned Jacobians are not necessarily common in FE computations and only arise when cells are badly scaled and/or near degenerate. Nevertheless, such cells do appear in graded meshes, when boundary layers need to be resolved, and in adaptive refinement. When reduced-precision computations need to be performed on such meshes we suggest a simple mixed-precision strategy: tailor the geometry precision to the cell conditioning and selectively employ higher-precision on low-quality cells.

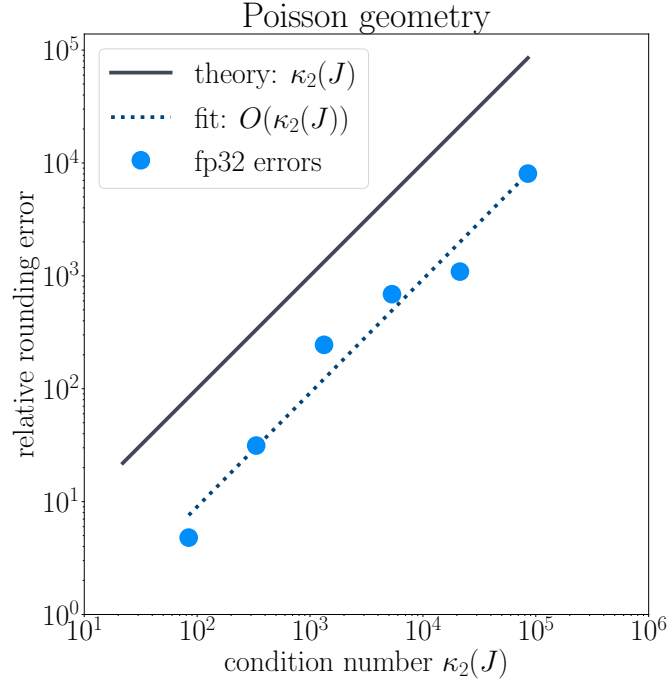


Figure 2: Relative rounding errors in the fp32 evaluation of the Poisson geometry as a function of the condition number of the reference map Jacobian. Fitting a line to the errors in the loglog plot yields the linear proportionality expected from Theorem 4.5.

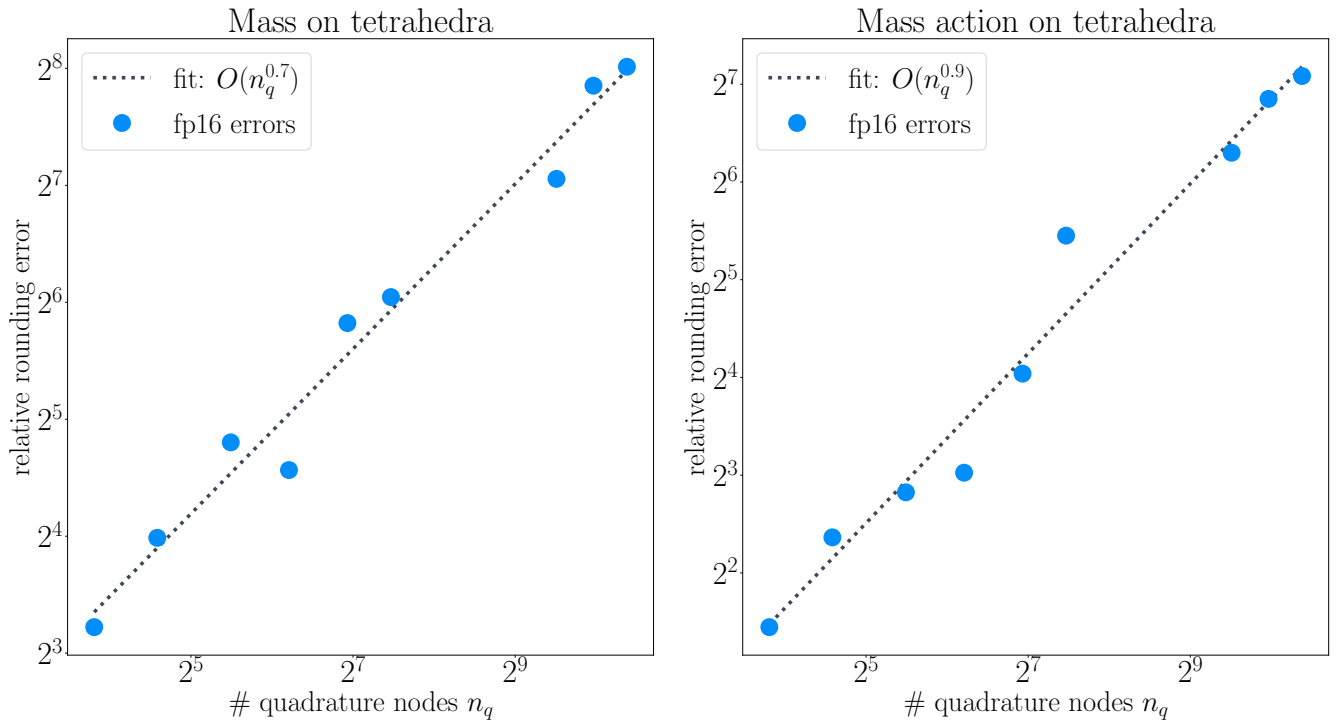


Figure 3: Relative rounding errors in mass kernel evaluations on tetrahedra versus the number of quadrature nodes n_q . Here the fp16 format is used in place of the precision u_q and single precision is used in everything else.

5.3 Errors in the accumulation of matrix-matrix products into the local tensors.

We now focus on the $O(u_q)$ error term in Theorems 4.8 and 4.9. Our objective here is to check whether we actually observe an error growth rate of $O(n_q)$. The $O(n_q)$ error growth is a direct consequence of (5) and is a worst-case error bound. However, it is well-known that rounding errors may behave stochastically leading to error cancellation and milder error growth rates [31]. For instance, for matrix-matrix products and rounding errors behaving as independent zero-mean random variable the rate would be $O(n_q^{1/2})$ [31]. Here we plan to determine which rates are observed in practice when running FE kernels.

For this purpose, we consider both mass kernels (bilinear form and action) on the tetrahedral mesh (results for hexahedral meshes are similar and thus not shown) and use single precision for storage, geometry, and polynomial/FE function evaluations so that $u_s = u_g = u_p = 2^{-24}$ and employ fp16 half precision for the matrix-matrix products so that $u_q = 2^{-11}$, cf. Table 1. These precision choices lead to a total rounding error dominated by the $O(u_q)$ term. We then monitor the relative rounding errors

$$\max_{k=1, \dots, \tilde{n}_K} \left(\frac{\|A^k - \hat{A}^k\|_{\max}}{u_q \|A^k\|_{\max}} \right), \quad \max_{k=1, \dots, \tilde{n}_K} \left(\frac{\|\mathbf{v}^k - \hat{\mathbf{v}}^k\|_{\infty}}{u_q \|\mathbf{v}^k\|_{\infty}} \right), \quad (128)$$

as a function of n_q . Results are shown in Figure 3. For mass actions we do observe a rate close to 1, indicating the expected error growth. However, for bilinear forms the rate is lower (0.7) indicating that some error cancellation is occurring. Checking the error behaviour on a cell-by-cell basis leads to varying rates between 0.5 and 1 so we can only conclude that the actual degree of error cancellation and growth rate with respect to n_q is cell- and form-dependent. This is not surprising, but it means that the only option when implementing fully low-precision kernels is to either determine experimentally the growth rate or to plan for the largest possible error growth.

We remark that the base-ten logarithm of the error indicates the number of digits lost in the computation. For fp16 this means that all precision is lost when the error reaches 2^1 so care must be taken for high polynomial degrees. For instance, from the left figure in Figure 3 we deduce that at polynomial degrees $p = 9, 10$ we already have less than 1 digit of accuracy. These consideration further motivate the use of mixed-precision accelerators that are able to efficiently compute the matrix-matrix products in higher precision.

5.4 Mixed-precision kernels: rounding errors.

We now study the accuracy of the hardware-accelerated mixed-precision kernels as described in Section 4.5. Namely, we use single precision for geometry, polynomial and FE function evaluations, and for the matrix-matrix products and their accumulation ($u_p = u_g = u_q = 2^{-24}$). For storage we use instead bf16 ($u_s = 2^{-8}$). Our aim is to validate the theory from Section 4 as well as establishing that these mixed-precision kernels yield indeed $O(u_s)$ errors where the hidden constant is essentially independent from the conditioning of geometry computations and polynomial and FE function evaluations as well as from the number of quadrature nodes and the polynomial degree.

We run mixed-precision kernels on all meshes and for all forms using either AVX512-bf16 or AMX-bf16 accelerators and we compare their error behaviour with a kernel almost fully run in fp16 half precision (except for the geometry which we have to run in fp32 to avoid underflow and much larger errors). We compute the relative rounding errors as

$$\max_{k=1, \dots, \tilde{n}_K} \left(\frac{\|A^k - \hat{A}^k\|_{\max}}{u_s \|A^k\|_{\max}} \right), \quad \max_{k=1, \dots, \tilde{n}_K} \left(\frac{\|\mathbf{v}^k - \hat{\mathbf{v}}^k\|_{\infty}}{u_s \|\mathbf{v}^k\|_{\infty}} \right), \quad (129)$$

where $u_s = 2^{-8}$ for the mixed-precision kernels using bf16 and $u_s = 2^{-11}$ for the fp16 kernels. Normalizing by the precision here is crucial for a fair comparison as it sanitizes the results from the choice of the half-precision format. Again, we would employ bf16 instead of fp16, but pure bf16 operations are not supported in the CPU. With this normalization the base-10 logarithm of the relative error is the number of digits lost in the computation which helps with the interpretation of the results.

Results are shown in Figure 4 for the mass forms and in Figure 5 for the Poisson forms where we plot the relative rounding errors versus the polynomial degree. These results match with what the theory predicts: while the fp16 errors grow with the polynomial degree (and thus n_q as well) and lose up to 2 digits of accuracy (out of 3.5), the relative rounding errors of the mixed-precision kernels are essentially $O(1)$ and constant, which implies that no digits have been lost. From Figure 2 we also know that as long as the condition number of the Jacobian is not larger than 10^5 then the errors arising from single-precision geometry computations are also negligible. Therefore, these mixed-precision strategies are an effective way of computing highly accurate kernels (given the precision) even at high polynomial degrees.

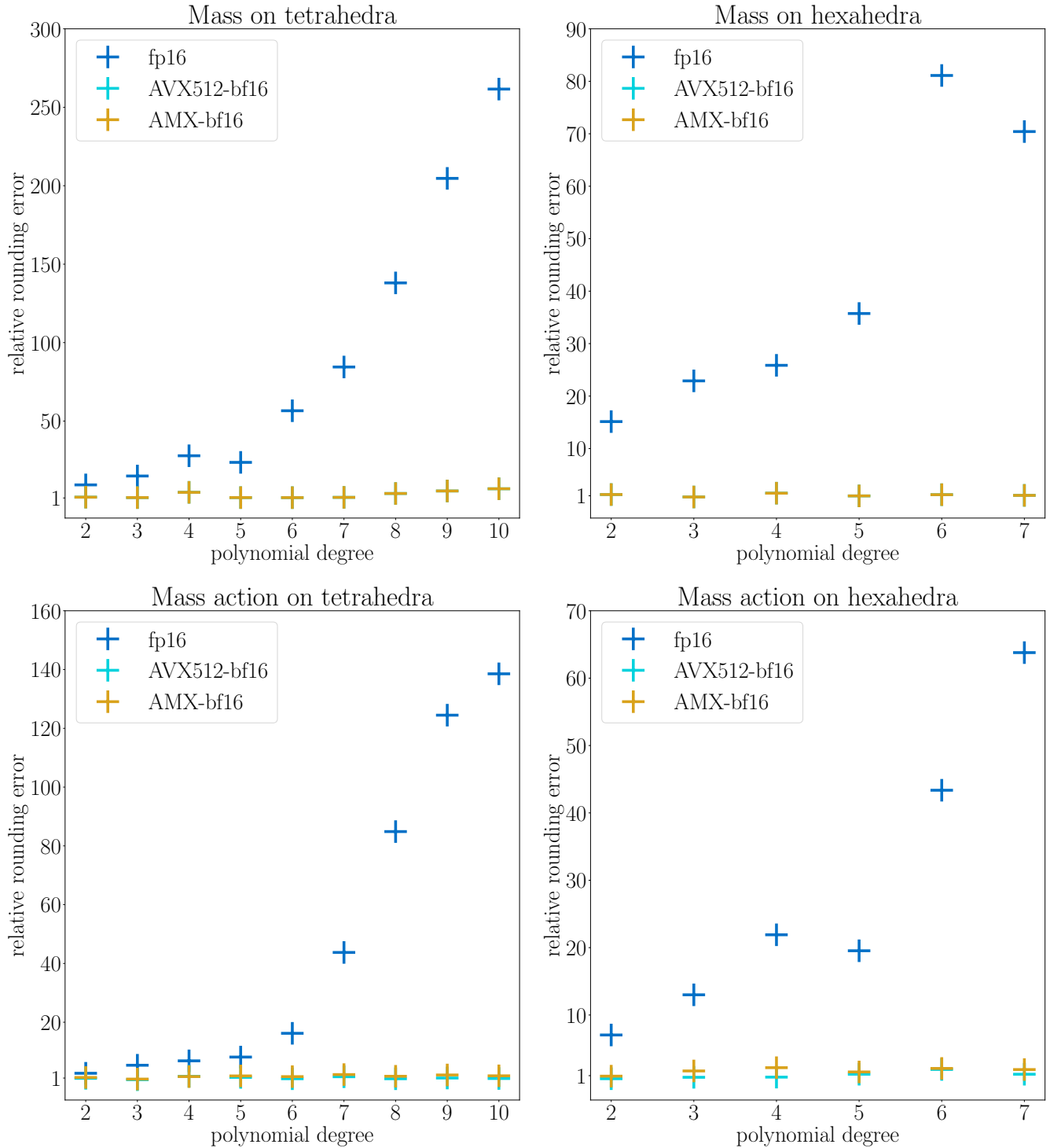


Figure 4: Relative rounding errors arising in the mass kernel evaluations via $fp16$ and $fp32/bf16$ mixed-precision plotted against the polynomial degree. The AVX512-bf16 and AMX-bf16 are almost overlapping. Note that the $fp16$ errors grow with p while the mixed-precision errors are constant.

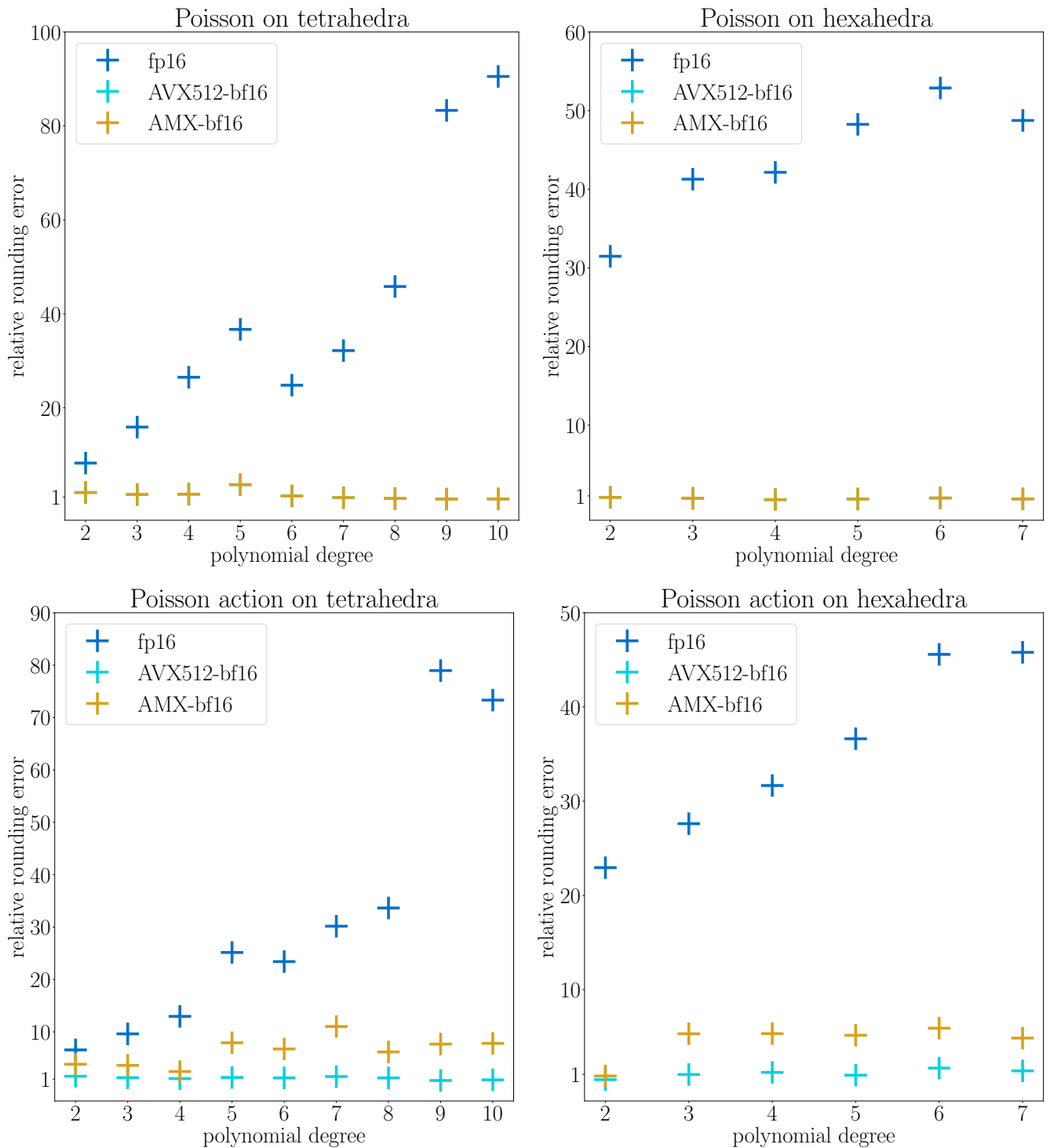


Figure 5: Relative rounding errors arising in the Poisson kernel evaluations via $fp16$ and $fp32/bf16$ mixed-precision plotted against the polynomial degree. The AVX512-bf16 and AMX-bf16 are almost overlapping for bilinear forms (top figures). The slight difference in the error constant of AVX512-bf16 and AMX-bf16 computations in the action kernels (bottom figures) is due to the different implementation: the AVX512-bf16 kernels are slightly more accurate since they evaluate FE functions using only single precision (cf. Appendix B).

Remark 5.2. In terms of absolute rounding errors the mixed-precision kernels are of the same order of the half-precision unit roundoff (roughly $2^{-8} \approx 0.0039$) which is still orders of magnitude larger than the error that would be obtained with single- or double-precision-only kernels (cf. Table 1). These considerations hold even after accounting for digit loss due to the larger error constants (see the fp16 results in Figures 4 and 5). Therefore, using the mixed-precision kernels is only suitable either when many digits of accuracy are not needed and/or after weighing this loss of accuracy against the speedups obtained (presented next).

5.5 Mixed-precision kernels: timings and speedup.

In this subsection we test the computational efficiency of the mixed-precision kernels described in Section 4.5. Our aim is to show that these kernels are appreciably more efficient than their pure single or double precision counterparts.

The kernels considered are the same as in the previous subsection, plus the addition of single- and double-precision-only kernels. We measure the kernel efficiency by the average per-cell CPU time taken by each kernel, excluding tabulation and quadrature rule construction which are performed offline once and for all for all cells. We then measure the speedup with respect to double precision by taking the ratio between the timings of each kernel and the corresponding double-precision timings.

Results are shown in Figure 6 for the mass forms and in Figure 7 for the Poisson forms. Firstly, we note that the reduced-/mixed-precision implementation presented in this paper is only beneficial for large enough polynomial degrees (larger than 4 or 5 for tetrahedra and larger than 2 or 3 for hexahedra). This behaviour is expected since our implementation is only really tailored to the higher polynomial degrees for which the advantages of AVX512 and AMX accelerators are more significant. Lower degrees imply a different cost and rounding error balance between the kernel components and would require a separate, tailored implementation which is outside the scope of this work. Secondly, we observe that the speedups are clearly dependent on the precision and accelerator choices:

- The (vectorized) single and half precision (dark and light blue respectively in the figures) are roughly up to twice and four times faster than double precision respectively. These are the typical improvements which we would expect to obtain by using lower-precision arithmetic (e.g., using half the digits results in twice the speed). We remark that these speedup factors do not occur in all reduced-precision applications so it is a positive result that they do occur for high-polynomial degree FE kernels.
- The vectorized mixed-precision AVX512-bf16 kernels (dark orange in the figures) yield varying results. For mass bilinear forms (Figure 6, top) they are as fast as half-precision with a factor-four speedup (while also being more accurate, recall Figure 4). This is also the maximum speedup that is theoretically achievable with AVX512-bf16 instructions (recall Section 2.3). For mass and Poisson actions (bottom of Figures 6 and 7) they are only slightly faster than single precision, and for Poisson bilinear forms they are as slow as double precision. We believe this performance may be due to a lack of CPU and compiler features. In fact, mixed-precision and bf16 instructions are limited if compared with typical AVX512 support and the compiler is unable to use these automatically. Even if we invoke these intrinsics by hand (which we do) this means that the full range of AVX512 kernel-wide compiler optimizations is unavailable here. Nevertheless, the four-times speedup obtained with mass bilinear forms is a promising result as it shows that these mixed-precision AVX512 kernels can indeed be as fast as half precision while being more accurate.
- The AMX-bf16 kernels (ocra in the figures) outperform all other kernels and yield large speedups. For high-degree polynomials, these kernels are over 32 times faster than double precision for mass bilinear forms on tetrahedra and up to 60 times faster on hexahedra. For all other forms they are between 8 and 16 times faster than vectorized double precision kernels. These speedups are remarkable since they go well beyond the usual factor-four obtainable with half precision and, for the mass bilinear forms, approach the theoretical maximum speedup obtainable with AMX instructions (i.e., $64\times$, cf. Section 2.3). Furthermore, the AMX kernels are not only faster than fp16 computations, but also more accurate (recall Figures 4 and 5). Additionally, we note that these kernels are not affected by the same slowdowns of the AVX512-bf16 kernels, likely because AMX-bf16 accelerators have a much higher throughput which more than compensates for the limited CPU/compiler bf16 support.

Remark 5.3. The results presented correspond as-is to the assembly of global tensors when discontinuous Lagrange basis functions are employed. We do not investigate numerically the assembly process of forms involving continuous Lagrange elements for the sake of brevity: continuous Lagrange elements only slightly affect timings and do not qualitatively affect rounding errors.

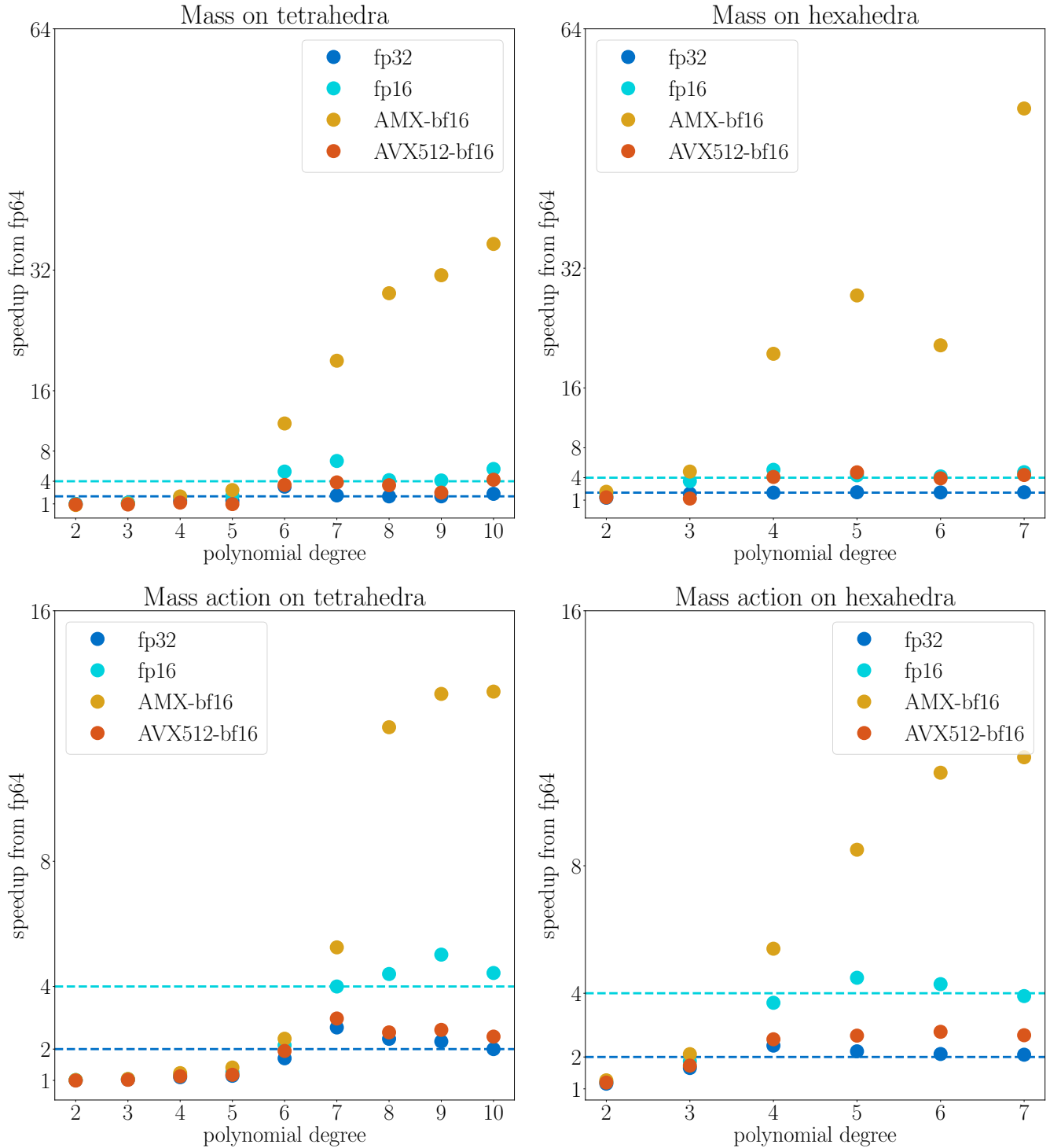


Figure 6: Computational speedup of the reduced- and mixed-precision mass kernels with respect to their double-precision equivalent versus the polynomial degree. The horizontal dashed lines correspond to the typical expected speedups obtainable with single and half-precision computations on CPUs (2 and 4 times respectively). The largest speedups are obtained by the AMX-bf16 kernels.

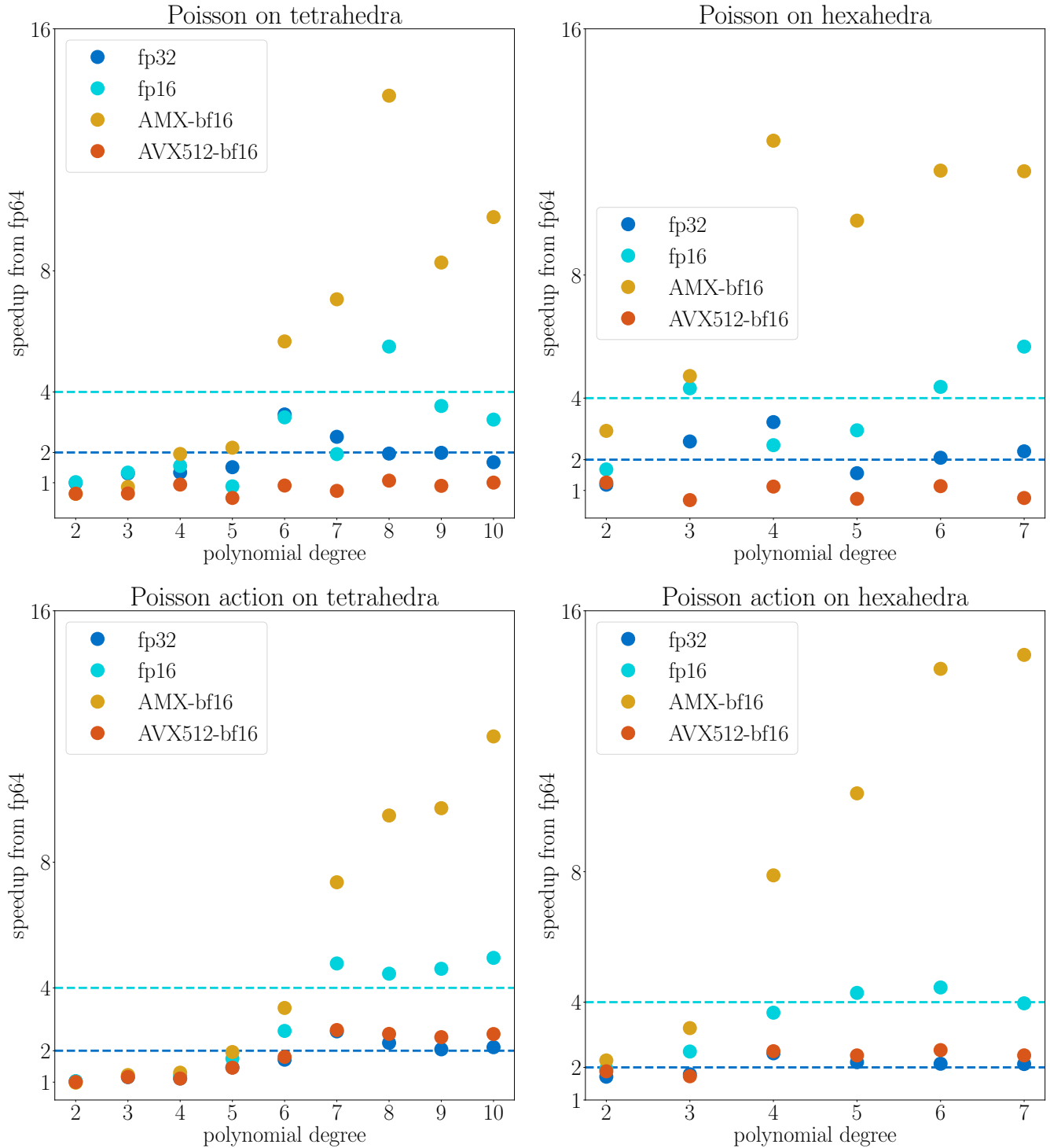


Figure 7: Computational speedup of the reduced- and mixed-precision Poisson kernels with respect to their double-precision equivalent versus the polynomial degree. The horizontal dashed lines correspond to the typical expected speedups obtainable with single and half-precision computations on CPUs (2 and 4 times respectively). The largest speedups are obtained by the AMX-bf16 kernels.

6 Conclusions

Artificial intelligence applications have been driving the development of computer chips that are optimized for parallel processing and reduced- and mixed-precision computations. While these hardware units are specifically tailored to computer vision and machine learning workloads, the exploitation of their parallel capabilities has also been shown to improve the efficiency of FE computations. However, the acceleration of the FE method via reduced- and mixed-precision implementations has received less attention and the effect of rounding errors in FE computations is underexplored in both theory and numerical practice. Indeed, there is no comprehensive rounding error analysis of the FE method that can guide reduced-precision implementations and ensure their accuracy.

This paper is a first step in the direction of closing this gap in the literature: We have derived the first rounding error analysis of FE kernels and assembly which also accounts for mixed-precision and hardware accelerated implementations. Furthermore, we have designed a mixed-precision implementation strategy which exploits mixed-precision matrix units to obtain FE kernels and assembly routines which are both performant and robust to half-precision computations. Indeed, the resulting algorithms are provenly half-precision accurate with an error constant that is independent from: the conditioning of FE basis function evaluations, the ill-posedness of the cell, the polynomial degree, and the number of quadrature nodes. Finally, we have presented the first single-/half-precision FE kernel implementations exploiting Intel AMX units. Numerical experimentation has shown that these kernels can be between 8 and 60 times faster than their double precision equivalents while being provenly more accurate than their fully half precision counterparts.

Additional investigation is still required to derive a comprehensive rounding error analysis and mixed-precision implementation of FE computations which also includes timestepping, linear and nonlinear solvers, and preconditioning strategies. For instance, an open research question is whether it is possible to design mixed-precision FE methods which benefit from the speedups resulting from reduced-precision computations while retaining high-precision accuracy.

Further implementation work is also required. In particular, the design of automatic architecture-specific code generation algorithms would be highly beneficial as it would lighten the implementation burden on the user, accelerate further research on the topic, and increase the adoption of reduced- and mixed-precision FE methods by the scientific community.

Acknowledgements MC was supported by the European Union Horizon research and innovation program under the Marie Skłodowska-Curie postdoctoral fellowship grant 101103593 (GEOLEARN). GNW was supported by Engineering and Physical Sciences Research Council grants EP/S005072/1, EP/W00755X/1 and EP/W026635/1.

References

- [1] A. Abdelfattah et al. “A survey of numerical linear algebra methods utilizing mixed-precision arithmetic”. *The International Journal of High Performance Computing Applications* 35.4 (2021), pp. 344–369.
- [2] J. Alvarez-Aramberri et al. “On round-off error for adaptive finite element methods”. *Procedia Computer Science* 9 (2012), pp. 1474–1483.
- [3] P. Amestoy et al. “Five-precision GMRES-based iterative refinement”. *SIAM Journal on Matrix Analysis and Applications* 45.1 (2024), pp. 529–552.
- [4] J. Andrej et al. “High-performance finite elements with MFEM”. *The International Journal of High Performance Computing Applications* (2024), p. 10943420241261981.
- [5] I. Babuška and G. Söderlind. “On roundoff error growth in elliptic problems”. *ACM Transactions on Mathematical Software (TOMS)* 44.3 (2018), pp. 1–22.
- [6] C. J. Balos, S. Roberts, and D. J. Gardner. “Leveraging mixed precision in exponential time integration methods”. *2023 IEEE High Performance Extreme Computing Conference (HPEC)*. IEEE, 2023, pp. 1–8.
- [7] K. Banaś, P. Płaszewski, and P. Macioł. “Numerical integration on GPUs for higher order finite elements”. *Computers & Mathematics with Applications* 67.6 (2014), pp. 1319–1344.
- [8] I. A. Baratta et al. *DOLFINx: the next generation FEniCS problem solving environment*. preprint, 2023. DOI: 10.5281/zenodo.10447666.
- [9] N. Beams et al. “High-order finite element method using standard and device-level batch GEMM on GPUs”. *2020 IEEE/ACM 11th Workshop on Latest Advances in Scalable Algorithms for Large-Scale Systems (ScalA)*. IEEE, 2020, pp. 53–60.

- [10] P. Blanchard, N. J. Higham, and T. Mary. “A class of fast and accurate summation algorithms”. *SIAM Journal on Scientific Computing* 42.3 (2020), A1541–A1557.
- [11] P. Blanchard et al. “Mixed precision block fused multiply-add: Error analysis and application to GPU tensor cores”. *SIAM Journal on Scientific Computing* 42.3 (2020), pp. C124–C141.
- [12] B. Burnett, S. Gottlieb, and Z. J. Grant. “Stability analysis and performance evaluation of additive mixed-precision Runge-Kutta methods”. *Communications on Applied Mathematics and Computation* 6.1 (2024), pp. 705–738.
- [13] E. Carson and N. Khan. “Mixed precision iterative refinement with sparse approximate inverse preconditioning”. *SIAM Journal on Scientific Computing* 45.3 (2023), pp. C131–C153.
- [14] C. Cecka, A. J. Lew, and E. Darve. “Assembly of finite element methods on graphics processors”. *International Journal for Numerical Methods in Engineering* 85.5 (2011), pp. 640–669.
- [15] P. G. Ciarlet. *The finite element method for elliptic problems*. SIAM, 2002.
- [16] M. Croci and M. B. Giles. “Effects of round-to-nearest and stochastic rounding in the numerical solution of the heat equation in low precision”. *IMA Journal of Numerical Analysis* 43.3 (2023), pp. 1358–1390.
- [17] M. Croci and G. R. de Souza. “Mixed-precision explicit stabilized Runge–Kutta methods for single-and multi-scale differential equations”. *Journal of Computational Physics* 464 (2022), p. 111349.
- [18] M. Croci et al. “Stochastic rounding: implementation, error analysis and applications”. *Royal Society Open Science* 9.3 (2022), p. 211631.
- [19] A. Dziekonski, P. Sypek, A. Lamecki, and M. Mrozowski. “Generation of large finite-element matrices on multiple graphics processors”. *International Journal for Numerical Methods in Engineering* 94.2 (2013), pp. 204–220.
- [20] M. Fasi, N. J. Higham, M. Mikaitis, and S. Pranesh. “Numerical behavior of NVIDIA tensor cores”. *PeerJ Computer Science* 7 (2021), e330.
- [21] M. Fasi et al. “Matrix multiplication in multiword arithmetic: Error analysis and application to GPU tensor cores”. *SIAM Journal on Scientific Computing* 45.1 (2023), pp. C1–C19.
- [22] G. Flegar, H. Anzt, T. Cojean, and E. S. Quintana-Orti. “Adaptive precision block-Jacobi for high performance preconditioning in the Ginkgo linear algebra software”. *ACM Transactions on Mathematical Software (TOMS)* 47.2 (2021), pp. 1–28.
- [23] I. Fried. “Discretization and round-off errors in the finite element analysis of elliptic boundary value problems and eigenvalue problems.” PhD thesis. Massachusetts Institute of Technology, 1971.
- [24] Z. Fu, T. J. Lewis, R. M. Kirby, and R. T. Whitaker. “Architecting the finite element method pipeline for the GPU”. *Journal of Computational and Applied Mathematics* 257 (2014), pp. 195–211.
- [25] V. Georgiou, C. Boutsikas, P. Drineas, and H. Anzt. “A mixed precision randomized preconditioner for the LSQR solver on GPUs”. *International Conference on High Performance Computing*. Springer. 2023, pp. 164–181.
- [26] C. Geuzaine and J.-F. Remacle. “Gmsh: A 3-D finite element mesh generator with built-in pre-and post-processing facilities”. *International Journal for Numerical Methods in Engineering* 79.11 (2009), pp. 1309–1331.
- [27] Z. J. Grant. “Perturbed Runge–Kutta methods for mixed precision applications”. *Journal of Scientific Computing* 92.1 (2022), p. 6.
- [28] A. Haidar et al. “Mixed-precision iterative refinement using tensor cores on GPUs to accelerate solution of linear systems”. *Proceedings of the Royal Society A* 476.2243 (2020), p. 20200110.
- [29] N. J. Higham. *Accuracy and Stability of Numerical Algorithms*. SIAM, 2002.
- [30] N. J. Higham. “The numerical stability of barycentric Lagrange interpolation”. *IMA Journal of Numerical Analysis* 24.4 (2004), pp. 547–556.
- [31] N. J. Higham and T. Mary. “A new approach to probabilistic rounding error analysis”. *SIAM Journal on Scientific Computing* 41.5 (2019), A2815–A2835.
- [32] N. J. Higham and T. Mary. “Mixed precision algorithms in numerical linear algebra”. *Acta Numerica* 31 (2022), pp. 347–414.

- [33] Intel[®] 64 and IA-32 Architectures Software Developer Manuals, August 2024 version. <https://www.intel.com/content/www/us/en/developer/articles/technical/intel-sdm.html>. Accessed: 2024-07-24.
- [34] Intel[®] Intrinsics Guide version 3.6.9. <https://www.intel.com/content/www/us/en/docs/intrinsics-guide/index.html>. Accessed: 2024-07-12.
- [35] I. C. Ipsen and R. Rehman. “Perturbation bounds for determinants and characteristic polynomials”. *SIAM Journal on Matrix Analysis and Applications* 30.2 (2008), pp. 762–776.
- [36] T. Isaac. “Recursive, parameter-free, explicitly defined interpolation nodes for simplices”. *SIAM Journal on Scientific Computing* 42.6 (2020), A4046–A4062.
- [37] G. Karniadakis and S. J. Sherwin. *Spectral/hp Element Methods for Computational Fluid Dynamics*. Oxford University Press, USA, 2005.
- [38] C. Kelley. “Newton’s method in mixed precision”. *SIAM Review* 64.1 (2022), pp. 191–211.
- [39] R. C. Kirby and A. Logg. “Efficient compilation of a class of variational forms”. *ACM Transactions on Mathematical Software (TOMS)* 33.3 (2007), 17–es.
- [40] M. Klöwer et al. “Fluid simulations accelerated with 16 bits: Approaching 4x speedup on A64FX by squeezing ShallowWaters.jl into Float16”. *Journal of Advances in Modeling Earth Systems* 14.2 (2022), e2021MS002684.
- [41] M. G. Knepley and A. R. Terrel. “Finite element integration on GPUs”. *ACM Transactions on Mathematical Software (TOMS)* 39.2 (2013), pp. 1–13.
- [42] A. G. Lewis et al. “Large-scale distributed linear algebra with tensor processing units”. *Proceedings of the National Academy of Sciences* 119.33 (2022), e2122762119.
- [43] F. Lopez and T. Mary. “Mixed precision LU factorization on GPU tensor cores: reducing data movement and memory footprint”. *The International Journal of High Performance Computing Applications* 37.2 (2023), pp. 165–179.
- [44] J. Maryška, M. Rozložník, and M. Tuma. “Schur complement reduction in the mixed-hybrid approximation of Darcy’s law: rounding error analysis”. *Journal of Computational and Applied Mathematics* 117.2 (2000), pp. 159–173.
- [45] S. F. McCormick, J. Benzaken, and R. Tamstorf. “Algebraic error analysis for mixed-precision multigrid solvers”. *SIAM Journal on Scientific Computing* 43.5 (2021), S392–S419.
- [46] R. J. Melosh. “Inherited error in finite element analyses of structures”. *Computers & Structures* 3.5 (1973), pp. 1205–1217.
- [47] R. J. Melosh and E. L. Palacol. *Manipulation errors in finite element analysis of structures*. Tech. rep. NASA, 1969.
- [48] R. Nicolaides. “On a class of finite elements generated by Lagrange interpolation”. *SIAM Journal on Numerical Analysis* 9.3 (1972), pp. 435–445.
- [49] E. Oktay and E. Carson. “Multistage mixed precision iterative refinement”. *Numerical Linear Algebra with Applications* 29.4 (2022), e2434.
- [50] W. Pazner, T. Kolev, and J.-S. Camier. “End-to-end GPU acceleration of low-order-refined preconditioning for high-order finite element discretizations”. *The International Journal of High Performance Computing Applications* 37.5 (2023), pp. 578–599.
- [51] J. M. Peña and T. Sauer. “On the multivariate Horner scheme”. *SIAM Journal on Numerical Analysis* 37.4 (2000), pp. 1186–1197.
- [52] I. Z. Reguly and M. B. Giles. “Finite element algorithms and data structures on graphical processing units”. *International Journal of Parallel Programming* 43 (2015), pp. 203–239.
- [53] J.-F. Rémacle, R. Gandham, and T. Warburton. “GPU accelerated spectral finite elements on all-hex meshes”. *Journal of Computational Physics* 324 (2016), pp. 246–257.
- [54] M. E. Rognes, R. C. Kirby, and A. Logg. “Efficient assembly of $H(\text{div})$ and $H(\text{curl})$ conforming finite elements”. *SIAM Journal on Scientific Computing* 31.6 (2010), pp. 4130–4151.
- [55] M. W. Scroggs, I. A. Baratta, C. N. Richardson, and G. N. Wells. “Basix: a runtime finite element basis evaluation library”. *Journal of Open Source Software* 7.73 (2022), p. 3982. DOI: 10.21105/joss.03982.

- [56] M. W. Scroggs, J. S. Dokken, C. N. Richardson, and G. N. Wells. “Construction of arbitrary order finite element degree-of-freedom maps on polygonal and polyhedral cell meshes”. *ACM Transactions on Mathematical Software* 48.2 (2022), 18:1–18:23. DOI: 10.1145/3524456.
- [57] R. Tamstorf, J. Benzaken, and S. F. McCormick. “Discretization-error-accurate mixed-precision multigrid solvers”. *SIAM Journal on Scientific Computing* 43.5 (2021), S420–S447.
- [58] F. Tisseur. “Newton’s method in floating point arithmetic and iterative refinement of generalized eigenvalue problems”. *SIAM Journal on Matrix Analysis and Applications* 22.4 (2001), pp. 1038–1057.
- [59] J. D. Trotter, J. Langguth, and X. Cai. “Targeting performance and user-friendliness: GPU-accelerated finite element computation with automated code generation in FEniCS”. *Parallel Computing* 118 (2023), p. 103051.
- [60] S. Utku and R. J. Melosh. “Solution errors in finite element analysis”. *Computers & Structures* 18.3 (1984), pp. 379–393.
- [61] A. J. Wathen. “Realistic eigenvalue bounds for the Galerkin mass matrix”. *IMA Journal of Numerical Analysis* 7.4 (1987), pp. 449–457.
- [62] J. H. Wilkinson. *Rounding Errors in Algebraic Processes*. SIAM, 2023.

A Rounding error analysis of finite element function evaluations.

The rounding error analysis of multivariate polynomial evaluations via Horner's method is known: In [51] the following result is proven:

Theorem A.1 ([51]). *Let $\phi(\mathbf{x})$ with $\mathbf{x} \in K \subset \mathbb{R}^d$ be a multivariate polynomial in d dimensions of total degree m . Let u be the working precision. There exist polynomial evaluation algorithms and an algorithm-dependent constant $c_\phi \geq 1$ which, assuming $(c_\phi m + d)u < 1$, evaluate $\phi(\mathbf{x})$ in finite precision yielding instead the quantity $\hat{\phi}(\mathbf{x})$ satisfying*

$$|\phi(\mathbf{x}) - \hat{\phi}(\mathbf{x})| \leq \gamma_{c_\phi m + d} \kappa(K, m, \phi) |\phi(\mathbf{x})|. \quad (130)$$

Here $\kappa(K, m, \phi)$ is the condition number of the evaluation problem which is algorithm-dependent. For the multivariate Horner scheme from [51] and the monomial basis, $c_\phi = 2$.

The above result holds for all polynomials and can thus be applied to any polynomial FE basis. However, for polynomials that are expressible as a product of monomials, such as Lagrange polynomials on simplices (cf. [48]) and quadrilaterals and hexahedra, the bound can be tightened:

Lemma A.2. *Let $\mathbf{x} \in K \subset \mathbb{R}^d$ and let $\phi(\mathbf{x})$ be a multivariate polynomial of total degree m which can be written in the form,*

$$\phi(\mathbf{x}) = w_\phi \prod_{i=1}^m \ell_i(\mathbf{x}), \quad (131)$$

where $w_\phi \in \mathbb{R}$ is known or pre-computed in exact arithmetic, and $\{\ell_i(\mathbf{x})\}_{i=1}^m$ are first-degree monomials. Assume that the evaluation of the monomials in finite precision yields instead $\hat{\ell}_i(\mathbf{x}) = \ell_i(\mathbf{x})(1 + \theta_r)$ with $|\theta_r| \leq \gamma_r$. Then, provided that $u(m(r+1)+1) < 1$, evaluating $\phi(\mathbf{x})$ as the product above yields instead $\hat{\phi}(\mathbf{x})$ satisfying

$$|\phi(\mathbf{x}) - \hat{\phi}(\mathbf{x})| \leq \gamma_{m(r+1)+1} |\phi(\mathbf{x})|. \quad (132)$$

Proof. Under the assumptions of the lemma it holds that

$$\hat{\phi}(\mathbf{x}) = \prod_{i=1}^{m+1} (1 + \delta_i) w_\phi \prod_{i=1}^m \hat{\ell}_i(\mathbf{x}) = (1 + \theta_{m+1})(1 + \theta_r)^m \left(w_\phi \prod_{i=1}^m \ell_i(\mathbf{x}) \right) = (1 + \theta_{m(r+1)+1}) \phi(\mathbf{x}). \quad (133)$$

Therefore

$$|\phi(\mathbf{x}) - \hat{\phi}(\mathbf{x})| \leq \gamma_{m(r+1)+1} |\phi(\mathbf{x})|, \quad (134)$$

which is the thesis. \square

Note that the result in Lemma A.2 is stronger than Theorem A.1 since there is no condition number appearing in the error bound, i.e., the evaluation problem in this case has perfect conditioning.

What about derivatives? Since derivatives of polynomials are polynomials, Theorem A.1 still applies, although it requires expressing the derivatives in terms of the multivariate monomial basis. We adopt a different strategy: under the assumptions of Lemma A.2, we can write the derivative of $\phi(\mathbf{x})$ as follows: for $s \in \{1, \dots, d\}$,

$$\partial_s \phi(\mathbf{x}) = w_\phi \sum_{j=1}^m (\partial_s \ell_j) \prod_{i \neq j} \ell_i(\mathbf{x}). \quad (135)$$

Here ∂_s denotes the partial derivative with respect to \mathbf{x}_s . Note that since ℓ_i are first-degree monomials, their derivatives are constants and can only attain the values ± 1 .

Lemma A.3. *Let the assumptions of Lemma A.2 hold. The evaluation of equation (135) yields $\widehat{\partial_s \phi}(\mathbf{x})$ satisfying:*

$$|\partial_s \phi(\mathbf{x}) - \widehat{\partial_s \phi}(\mathbf{x})| \leq \gamma_{(m-1)(r+1)} \sum_{j=1}^m \left| \frac{\phi(\mathbf{x})}{\ell_j(\mathbf{x})} \right|, \quad (136)$$

$$\max_{\mathbf{x} \in K} |\partial_s \phi(\mathbf{x}) - \widehat{\partial_s \phi}(\mathbf{x})| \leq \gamma_{(m-1)(r+1)} \kappa(\partial_s \phi) \max_{\mathbf{x} \in K} |\partial_s \phi(\mathbf{x})|, \quad (137)$$

$$\text{where } \kappa(\partial_s \phi) = \frac{\max_{\mathbf{x} \in K} \sum_{j=1}^m |\phi(\mathbf{x}) / \ell_j(\mathbf{x})|}{\max_{\mathbf{x} \in K} |\partial_s \phi(\mathbf{x})|} \geq 1. \quad (138)$$

Proof. Since $\partial_s \ell_j = \pm 1$, these terms are exactly representable and their product is always exact. Therefore, each term in the sum in (135) is of the same form as (131) with one less term in the product and without the final multiplication by w_ϕ . It thus holds that

$$\widehat{(\partial_s \ell_j)} \prod_{i \neq j}^m \ell_i(\mathbf{x}) = (1 + \theta_{(m-1)(r+1)-1}) (\partial_s \ell_j) \prod_{i \neq j}^m \ell_i(\mathbf{x}). \quad (139)$$

Here we have used the same argument as for equation (133). Hence, we have that

$$\widehat{\partial_s \phi}(\mathbf{x}) = (1 + \theta_{(m-1)(r+1)}) w_\phi \sum_{j=1}^m (\partial_s \ell_j) \prod_{i \neq j}^m \ell_i(\mathbf{x}) (1 + \theta_{m-1}^j), \quad (140)$$

where we write $(1 + \theta_{m-1}^j)$ to indicate that the rounding errors in the sum are j -dependent. From the above and using $|\partial_s \ell_j| = 1$ we obtain the bound

$$|\partial_s \phi(\mathbf{x}) - \widehat{\partial_s \phi}(\mathbf{x})| \leq \gamma_{(m-1)(r+1)} \sum_{j=1}^m \left| w_\phi \prod_{i \neq j}^m \ell_i(\mathbf{x}) \right| = \gamma_{(m-1)(r+1)} \sum_{j=1}^m \left| \frac{\phi(\mathbf{x})}{\ell_j(\mathbf{x})} \right|, \quad (141)$$

which is equation (136). Taking the maximum over all $\mathbf{x} \in K$ (recall that K is compact by assumption) and multiplying and dividing by $\max_{\mathbf{x} \in K} |\partial_s \phi(\mathbf{x})|$ yields equation (137). The bound $\kappa(\partial_s \phi) \geq 1$ is proven by applying the triangle inequality to equation (135) and using again $|\partial_s \ell_j| = 1$. This final step concludes the proof. \square

It is straightforward to extend the error bounds for basis function evaluations to bounds for finite element function evaluations:

Lemma A.4. *Let \tilde{K} be a reference cell and let $V_{\tilde{K}} = \text{span}(\Phi)$ where $\Phi(\tilde{\mathbf{x}}) = [\phi_i(\tilde{\mathbf{x}})]_{i=1}^{n_\phi}$ and its entries are polynomials which satisfy the assumptions of Lemmas A.2 and A.3. For $\mathbf{z} = [z_i]_{i=1}^{n_\phi}$, let $z_h = \mathbf{z}^T \Phi(\tilde{\mathbf{x}}) \in V_{\tilde{K}}$ and assume that $u(m(r+2) + n_\phi) < 1$. Evaluating z_h and $\partial_s z_h$ in precision u yields \hat{z}_h and $\widehat{\partial_s z_h}$ respectively satisfying*

$$\max_{\tilde{\mathbf{x}} \in \tilde{K}} |z_h - \hat{z}_h| \leq \gamma_{n_\phi + m(r+1) + 1} \kappa(V_{\tilde{K}}) \|\mathbf{z}\|_\infty, \quad (142)$$

$$\max_{\tilde{\mathbf{x}} \in \tilde{K}} |\partial_s z_h - \widehat{\partial_s z_h}| \leq \gamma_{n_\phi + (m-1)(r+1)} \kappa(\partial_s \Phi) \kappa(\partial_s V_{\tilde{K}}) \|\mathbf{z}\|_\infty, \quad (143)$$

$$\text{where } \kappa(V_{\tilde{K}}) := \max_{\tilde{\mathbf{x}} \in \tilde{K}} \|\Phi(\tilde{\mathbf{x}})\|_1, \quad \kappa(\partial_s V_{\tilde{K}}) := \max_{\tilde{\mathbf{x}} \in \tilde{K}} \|\partial_s \Phi(\tilde{\mathbf{x}})\|_1, \quad \text{and } \kappa(\partial_s \Phi) := \max_{i=1, \dots, n_\phi} \kappa(\partial_s \phi_i). \quad (144)$$

Proof. Since $z_h = \mathbf{z}^T \Phi$ and $\partial_s z_h = \mathbf{z}^T (\partial_s \Phi)$, we can apply the error bound for inner products (cf. equation (3)) and Lemma A.2 to obtain the first bound:

$$\max_{\tilde{\mathbf{x}} \in \tilde{K}} |z_h - \hat{z}_h| \leq (\gamma_{n_\phi} + \gamma_{m(r+1)+1} + \gamma_{n_\phi} \gamma_{m(r+1)+1}) \max_{\tilde{\mathbf{x}} \in \tilde{K}} |\mathbf{z}^T \Phi| \leq \gamma_{n_\phi + m(r+1) + 1} \|\mathbf{z}\|_\infty \max_{\tilde{\mathbf{x}} \in \tilde{K}} \|\Phi\|_1. \quad (145)$$

Here we have used the relation $\gamma_a + \gamma_b + \gamma_a \gamma_b \leq \gamma_{a+b}$, cf. Lemma 2.2. Similarly, combining the error bound (3) for inner products with Lemma A.3 yields the second bound in the lemma and concludes the proof:

$$\max_{\tilde{\mathbf{x}} \in \tilde{K}} |\partial_s z_h - \widehat{\partial_s z_h}| \leq \gamma_{n_\phi + (m-1)(r+1)} \kappa(\partial_s \Phi) \kappa(\partial_s V_{\tilde{K}}) \|\mathbf{z}\|_\infty. \quad (146)$$

\square

We now specialize the above results to Lagrange elements over reference simplices or boxed cells:

Lemma A.5. *Let \tilde{K} be a d -dimensional reference simplex or boxed cell and let $V_{\tilde{K}} = \text{span}(\Phi)$, where the entries of Φ form the degree- p nodal Lagrange reference basis over \tilde{K} . Then, if u is sufficiently small, the evaluation of $\phi_i(\tilde{\mathbf{x}})$ and its derivatives in precision u satisfy, for all i and for all $\tilde{\mathbf{x}} \in \tilde{K}$, the bounds*

$$|\phi_i(\tilde{\mathbf{x}}) - \hat{\phi}_i(\tilde{\mathbf{x}})| \lesssim d p u |\phi_i(\tilde{\mathbf{x}})|, \quad (147)$$

$$\max_{\tilde{\mathbf{x}} \in \tilde{K}} |\partial_s \phi_i(\tilde{\mathbf{x}}) - \widehat{\partial_s \phi}_i(\tilde{\mathbf{x}})| \lesssim d p u \kappa(\partial_s \phi_i) \max_{\tilde{\mathbf{x}} \in \tilde{K}} |\partial_s \phi_i(\tilde{\mathbf{x}})|, \quad (148)$$

Furthermore, the evaluation of a function $z_h(\tilde{\mathbf{x}}) = \mathbf{z}^T \Phi(\tilde{\mathbf{x}})$ and its derivatives satisfy the bounds

$$\max_{\tilde{\mathbf{x}} \in \tilde{K}} |z_h - \hat{z}_h| \lesssim p^d u \kappa(V_{\tilde{K}}) \|\mathbf{z}\|_\infty, \quad (149)$$

$$\max_{\tilde{\mathbf{x}} \in \tilde{K}} |\partial_s z_h - \widehat{\partial_s z_h}| \lesssim p^d u \kappa(\partial_s \Phi) \kappa(\partial_s V_{\tilde{K}}) \|\mathbf{z}\|_\infty. \quad (150)$$

Proof. Nodal Lagrange finite elements satisfy the assumptions of Lemmas A.2, A.3, and A.4, see, e.g., [15, Section 2] and [48]. The value of n_ϕ for these elements is well known: we have $n_\phi = (p+1)^d$ if \tilde{K} is a boxed cell and $n_\phi = \frac{1}{d!} \prod_{j=1}^d (p+j)$ if \tilde{K} is a simplex. In both cases, $n_\phi = O(p^d)$. Similarly, it is well known that $m = pd$ for boxed cells and $m = p$ for simplices. For boxed cells we have $r = O(1)$ since each monomial is in the form $\ell_i(\tilde{\mathbf{x}}) = \tilde{x}_j - \tilde{y}_j$ for some $j \in \{1, \dots, d\}$ and some $\tilde{\mathbf{y}} \in \tilde{K}$, and therefore no more than $O(1)$ roundoffs affect each monomial evaluation. For simplices monomials include coordinates from all dimensions (cf. [48]) so we have $r = O(d)$. Therefore, for both simplices and boxed cells we have $O(mr) = O(pd)$. We can consequently replace all $\gamma_{O(mr)}$ terms with $O(pdu)$ and all $\gamma_{O(n_\phi+mr)}$ terms with $O(p^d u)$ and the corollary is proved. \square

B Implementation details.

We found the overall bf16 intrinsics and compiler support to be limited. To circumvent these limitations we made some implementation choices which we highlight here for the sake of reproducibility:

- We implement mixed-precision matrix and dot products by employing Intel intrinsics [34]. Indeed, compilers¹² are unable to automatically use the mixed-precision fp32/bf16 AVX and AMX accelerators available in the processor.
- The processor and the Intel intrinsics [34] have limited vectorization support for bf16: the only operations available are casting to and from single precision and an fp32/bf16 mixed-precision entrywise dot product. When a pure bf16 operation is needed we perform it by casting to and from fp16 which has full vectorization support. The fp16 format has a higher precision, but a narrower range, therefore this casting increases the chances of underflow/overflow. We did not find this to be problematic in our experiments.
- We use bit manipulations to cast fp16 to bf16 (with full subnormal support) and we employ Intel AVX512 intrinsics for casting from fp32 to bf16 [34]. The reason is that we found the compiled version of these operations to be either unnecessarily slow or bugged.
- In the AMX-bf16 and AVX512-bf16 kernels we use mixed-precision accelerators for the accumulation of matrix-matrix products into the local tensors. However, only the AMX kernels employ these accelerators for the FE function evaluations as well. In the AVX512-bf16 kernels these evaluation are performed entirely in (vectorized) single precision. The reason is that while AMX-bf16 accelerators are much faster than vectorized computations in any precision, the evaluations performed with AVX512-bf16 accelerators are sometimes slower than their fully single precision equivalents (for results and a discussion about this issue see Section 5.5).

¹²Not just g++ (GCC version 14.2.0). The same applies to all other compilers we tried: the clang++ compiler (LLVM version 18.1.8) and the Intel icpx compiler (Intel OneAPI version 2024.2.0).